JGR Oceans

RESEARCH ARTICLE
10.1029/2019JC015662

Warm Atlantic Water Explains Observed Sea Ice Melt Rates North of Svalbard

Pedro Duarte[1], Arild Sundfjord[1], Amelie Meyer[1,2], Stephen R. Hudson[1], Gunnar Spreen[3], and Lars H. Smedsrud[4]

[1]Norwegian Polar Institute, Fram Centre, Tromsø, Norway, [2]ARC Centre of Excellence for Climate Extremes, IMAS University of Tasmania, Hobart, Tasmania, Australia, [3]Institute of Environmental Physics, University of Bremen, Bremen, Germany, [4]Geophysical Institute, Bjerknes Centre for Climate Research, University of Bergen, Bergen, Norway

Key Points:
- Most of the sea ice entering the area known as Whalers Bay, in the NW of Svalbard, melts in less than a month, keeping it almost ice-free
- Melting rates larger than 1.5 m month^{-1} result from a combination of the presence of warm Atlantic water and storm-enhanced mixing
- In the absence of storms, estimated high sea ice melting rates require ocean surface temperature above 5°C

Supporting Information:
- Supporting Information S1
- Figure S1
- Figure S2
- Figure S3
- Figure S4
- Figure S5

Correspondence to:
P. Duarte,
pedro.duarte@npolar.no

Citation:
Duarte, P., Sundfjord, A., Meyer, A., Hudson, S. R., Spreen, G., & Smedsrud, L. H. (2020). Warm Atlantic water explains observed sea ice melt rates north of Svalbard. *Journal of Geophysical Research: Oceans*, *125*, e2019JC015662. https://doi.org/10.1029/2019JC015662

Received 16 SEP 2019
Accepted 4 JUN 2020
Accepted article online 11 JUL 2020

Abstract Warm Atlantic water (AW) that flows northward along the Svalbard west coast is thought to transport enough heat to melt regional Arctic sea ice effectively. Despite this common assumption, quantitative requirements necessary for AW to directly melt sea ice fast enough under realistic winter conditions are still poorly constrained. Here we use meteorological data, satellite observations of sea ice concentration and drift, and model output to demonstrate that most of the sea ice entering the area over the Yermak Plateau melts within a few weeks. Simulations using the Los Alamos Sea Ice Model (CICE) in a 1-D vertically resolved configuration under a relatively wide range of in situ observed atmospheric and ocean forcing show a good fit to observations. Simulations require high-frequency atmospheric forcing data to accurately reproduce vertical heat fluxes between the ice or snow and the atmosphere. Moreover, we switched off hydrostatic equilibrium to properly reproduce ice and snow thickness when observations showed that ice had a negative freeboard, without surface flooding and snow-ice formation. This modeling shows that realistic melt rates require a combination of warm near-surface AW and storm-induced ocean mixing. However, if AW is warmer than usual (>5°C), then lower mixing rates are sufficient. Our results suggest that increased winter storm frequency and increased heat content of the AW may work together in reducing future sea ice cover in the Eurasian basin.

Plain Language Summary Northwest of Svalbard, north of Norway, an area known as Whalers Bay stays ice-free in winter despite the negative air temperatures. It has been assumed that this open water is maintained by inflow of warm Atlantic water (AW) along Svalbard's west coast; however, this mechanism has never been demonstrated quantitatively. We combine observations and results from modeling to calculate the rate of ice melting necessary to keep Whalers Bay ice-free and the amount of heat that must be transferred from the ocean to the ice to sustain such melting. We conclude that the presence of AW combined with the occurrence of storms releases the amount of heat necessary to keep the area ice-free. When the AW is close to the surface and its temperature is above about 5°C, storms are no longer necessary to enhance heat transfer and produce the required melting. Since the amount of heat transported by the AW and the storm frequency have been increasing over several decades, we expect that the ice-free area will increase in the future, affecting air-sea-ice fluxes, water mass transformation, marine ecology, sea ice cover, and commercial activity including transportation and fishing.

1. Introduction

The sea ice cover in the Arctic Ocean is in transition to a new, thinner regime. This entails a decrease in the ratio of sea ice thickness to snow load, which increases the likelihood of sea ice flooding events (Granskog et al., 2017; Maslanik et al., 2007; Merkouriadi, Liston, et al., 2020; Stroeve et al., 2012). Ice thinning implies that the ice pack will be more fractured and mobile (Graham et al., 2019; P. Itkin et al., 2017; Spreen et al., 2011), which will increase atmosphere-ocean interaction, in turn enhancing ocean mixing and, potentially, upper-ocean vertical heat fluxes. It is therefore important to understand the interaction between the atmosphere, snow, sea ice, and ocean in this evolving thin-ice regime and to assess the quality of modeling tools which have mostly been developed based on older in situ observations from times when the ice cover was thicker. The Eurasian Basin has experienced large sea ice loss in recent years (Polyakov et al., 2017). There has been a larger winter sea ice loss north of Svalbard than elsewhere in the Arctic Basin (Onarheim et al., 2014), in line with changes taking place in the Barents Sea (Årthun et al., 2012; Lind

et al., 2018). The thin and highly variable ice cover in this region should thus be useful for model testing and development.

The Fram Strait Branch of the North Atlantic Current is the major carrier of oceanic heat to the Arctic Basin and likely responsible for the ice-free conditions in the eastern Fram Strait (roughly between 0° and 10°E longitude and as far north as ~80°N latitude) (Schauer et al., 2004; Spielhagen et al., 2011) (Figure 1) and the recent decline in sea ice cover north of Svalbard (Onarheim et al., 2014; Tetzlaff et al., 2014). Furthermore, the heat transported by the Atlantic water (AW) with this current appears to be increasing and, thereafter, accelerating sea ice melting in the Eastern Nansen Basin (Polyakov et al., 2017).

In the Eastern Fram Strait and over the southern part of Yermak Plateau, AW is typically found between 50 and ~600 m depth, often with a thin layer of colder and fresher Arctic Water and/or sea ice melt water above it (Meyer, Sundfjord, et al., 2017; Spielhagen et al., 2011). During winter, heat from warm AW is the only factor that can melt ice in this region due to the lack of incoming shortwave radiation and predominantly negative air temperatures (Onarheim et al., 2014; Walczowski & Piechura, 2011). There is evidence for a significant warming of the uppermost AW in the Fram Strait Branch during the past ~120 years (Spielhagen et al., 2011), amounting to about 2°C since the 1960s (Muilwijk et al., 2018). This warming is in line with a trend of +0.6°C per decade at 78°50′N for the period 1997–2010 from a mooring time series (Beszczynska-Möller et al., 2012) and a trend of +0.3°C per decade for the period 1979–2012 found by Onarheim et al. (2014), based on data collected west of Sørkapp—the southern tip of Spitsbergen (~76°33′ N). Therefore, it is likely that the role of AW in sea ice melting will increase if these warming trends persist.

Recent observations (Menze et al., 2019) and numerical model simulations (Crews et al., 2019; Koenig et al., 2017) have provided a more detailed understanding of the AW pathways across the Yermak Plateau (Figure 1b). The Svalbard Branch consistently transports ~1 Sv (1 Sv = 10^6 m^3 s^{-1}) over the shallower part of the plateau all year. The Yermak Pass Branch, which follows a slight depression across the central part of the plateau, shows a distinct seasonality where summer transport (~1.3 Sv) is similar to the Svalbard Branch but autumn and winter transport is much larger (~2.4 Sv), indicating that this pathway is the most important for annual AW volume flux from the West Spitsbergen Current into the Arctic Basin (Crews et al., 2019).

Upper-ocean heat fluxes in the AW inflow area north of Svalbard vary greatly over small distances as well as temporally. The upper part of the continental slope, where the core of the AW inflow is found, stands out as an area with high vertical heat fluxes. During the N-ICE2015 expedition (Granskog et al., 2018), heat fluxes measured in the ice-ocean boundary layer varied between near zero during calm periods with no wind in the deep basin and a 15 min average of almost 600 W m^{-2} during storms over shallow AW (Meyer, Fer, et al., 2017; Peterson et al., 2017). Heat fluxes of 400 W m^{-2} were observed frequently over AW north of Svalbard (Provost et al., 2017). Meyer, Fer, et al. (2017) identified the following key conditions that explain changes in the magnitude of ocean heat fluxes in the area north of Svalbard during the N-ICE2015 expedition: storms combined with the presence of shallow AW, the presence of shallow AW alone, and storms alone, in contrast to the deep Nansen Basin where storms and shallow AW were absent. They estimated the relative importance of each set of conditions relative to the deep Nansen Basin to follow the ratio 6:5:2:1, suggesting that the effect of storms combined with shallow AW increased ocean heat fluxes sixfold. Even as far east as 30°E, Renner et al. (2018) reported vertical heat flux estimates over the AW boundary current exceeding 100 W m^{-2} for week-long periods extending well into winter.

The role of oceanic heat fluxes in the energy budget of the new thinner Arctic sea ice is a key question in polar oceanography (Carmack et al., 2015; Polyakov et al., 2013). There is compelling evidence for the role of AW in melting Arctic sea ice in the Eastern Fram Strait and over the southern part of the Yermak Plateau based on (i) near absence of sea ice in winter, (ii) large sea ice loss in the Eurasian Basin in recent years, and (iii) increasing heat content of AW (e.g., Onarheim et al., 2014; Polyakov et al., 2017; Walczowski & Piechura, 2011). However, the role of oceanic heat fluxes in the energy budget of this area has yet to be quantified using direct observations and detailed simulations.

The main goal of this study is to quantify the role of the AW in sea ice melting in the region north of Svalbard utilizing observed atmospheric forcing at intra-annual time scales. Secondary objectives include the calculation of sea ice energy budgets in a wider region north of Svalbard, contrasting various hydrographic and

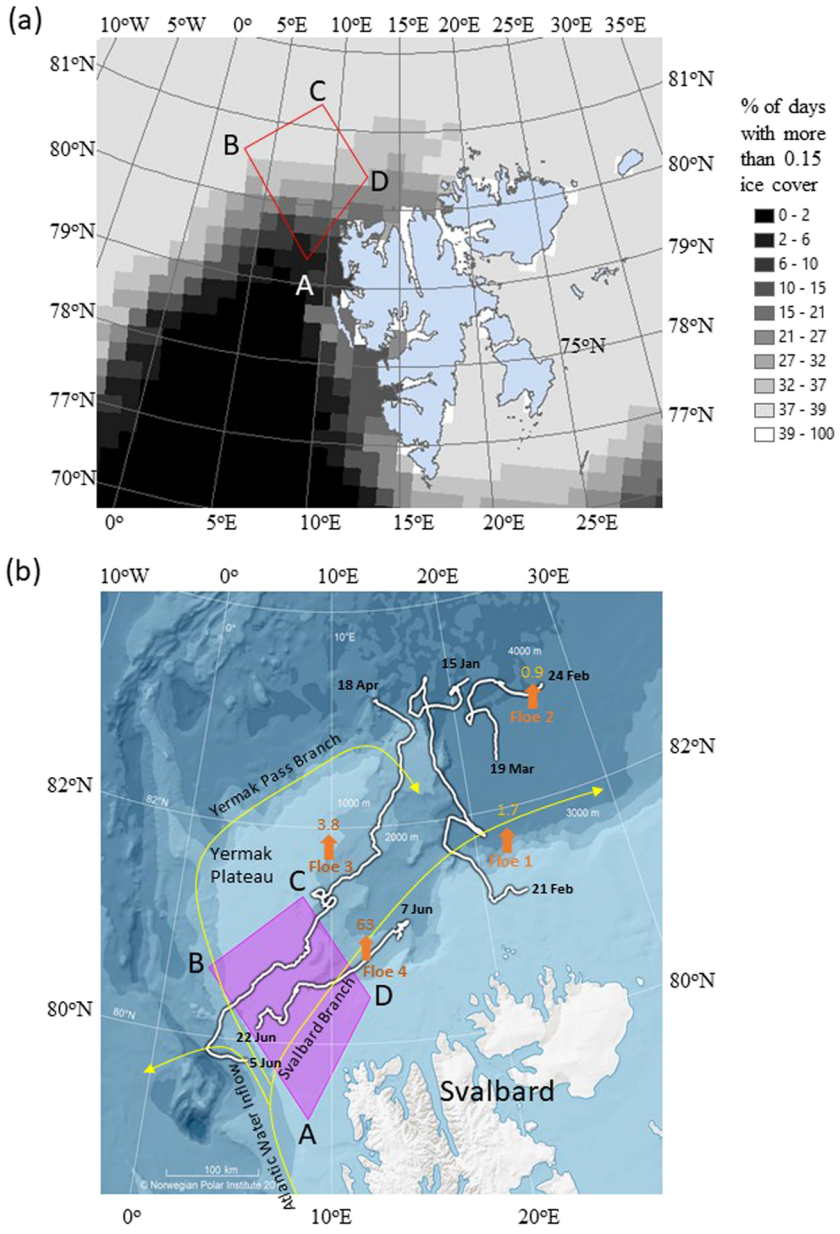

Figure 1. (a) Mean percentage of ice-covered days for April over the period 1985–2015. Chart derived from daily sea ice concentration data provided by the National Snow and Ice Data Center, USA. Ice frequency is defined as the frequency of occurrence of sea ice concentration values equal or higher than 0.15. A value of 100% indicates areas where every single day sea ice concentrations were equal or higher than 0.15, while a value of 0% indicates areas where such sea ice concentrations have never been observed (data source: M. Itkin et al., 2014). The polygon in the northwest corner of Svalbard was used to calculate sea ice melting from satellite data (see section 2.2) and is defined by the following Coordinates A (8.8°E, 79.3°N), B (2.5°E, 80.6°N), C (8.1°E, 81.3°N), and D (12.3°E, 80.4°N) (center grid coordinates). (b) RV Lance drifts (white lines) between 15 January and 22 June 2015 during the N-ICE2015 expedition, from the Nansen Basin and across the Yermak Plateau, with underlying topography. Start and end dates of the drifts are given for the four ice floes monitored during the N-ICE2105 expedition. Vertical arrows with numbers are average heat fluxes (W m^{-2}) measured at the under-ice boundary layer during the drift of the four ice floes (Peterson et al., 2017). The yellow arrows show the approximate main pathways of the Atlantic water (Yermak and Svalbard pass branches) (refer to text).

meteorological conditions in order to gain further insights into the relative importance of AW in those budgets. We use satellite data of sea ice concentration and drift to establish the role of local melting in explaining the near absence of sea ice around the NW corner of Svalbard, sometimes referred to as Whalers Bay. Estimated melting rates are then correlated with atmospheric observations to identify the

contribution of storms to melting. We use observations from the N-ICE2015 expedition to assess how well the Los Alamos Sea Ice Model (CICE) handles such highly variable conditions with respect to sea ice/snow thickness and temperature and large and rapid changes in energy balance, due to storms and the presence of shallow AW. Afterward, the CICE model is used to simulate various scenarios, attempting to establish the relative role of weather and oceanographic conditions in ice melting in Whalers Bay. Finally, empirical and model results are synthesized.

2. Methodology

Our study of the thermodynamic processes north of Svalbard uses detailed field observations (section 2.1) and remote sensing products of sea ice and the ocean surface layer as well as atmospheric reanalysis data (section 2.2). Some of these observations are used to force and evaluate the simulations carried out with the CICE model (section 2.3).

2.1. Field Observations From N-ICE2015

The field observations were collected in winter and spring 2015 during the N-ICE2015 expedition with RV *Lance*. Four drifting ice camps, referred to as Floes 1 to 4, were established in the southern Nansen Basin of the Arctic Ocean to collect data sets of the atmosphere-snow-ice-ocean-ecosystem interactions in a thinner Arctic sea ice regime (Granskog et al., 2018) (Figure 1b). This study uses the suite of field observations listed in Table 1, for (i) model initialization, (ii) model forcing, and (iii) model evaluation. For model forcing, we interpolated data sets linearly to fill in gaps and/or to properly synchronize with model data input routines. All model forcing and evaluation data were obtained on, in, and below the same ice floe, within a radius of a few hundred meters. Most of the observations are described in detail in other papers (Cohen et al., 2017, for meteorological observations; Gallet et al., 2017, and Merkouriadi, Gallet, et al., 2017, for spring and winter snow conditions, respectively; P. Itkin et al., 2017, and Provost et al., 2017, for sea ice and snow observations based on Ice Mass Balance (IMB) Buoys; Meyer, Fer, et al., 2017, Meyer, Sundfjord, et al., 2017, and Peterson et al., 2017, for hydrographic observations and ocean heat fluxes; Walden, Hudson, et al., 2017, for snow-atmosphere sensible and latent heat fluxes). These data are publicly available (see Table 1 and references therein). Water masses definitions follow the Rudels et al. (2000) classification and are shown in Meyer, Sundfjord, et al. (2017) as a temperature-salinity diagram (their Figure 5a) and a section plot (their Figure 6). AW was defined as having a potential density anomaly $27.70 < \sigma_0 < 27.97$ kg m^{-3} and a potential temperature $\theta > 2$°C. The upper boundary for AW was found as shallow as 30 m depth and as deep as 300 m.

For the purposes of visualizing both observational and model data, we calculate freeboard with the Archimedes buoyancy principle, based on snow and ice thicknesses and densities and on seawater density. Details on how the calculations were performed and which parameters were used are given in supporting information Text S1. Calculations were based on Assur (1958), Millero and Poisson (1981), Unesco (1983), Notz (2005), Hunke et al. (2015), and Provost et al. (2017).

2.2. Remote Sensing, Reanalysis Data, and Deduced Melt Rates

We use satellite sea ice data and hindcasts from the global 1/12° real time operational system (PSY4), developed at Mercator Ocean for the Copernicus Marine Environment Monitoring Service (http://marine.copernicus.eu/) in addition to atmospheric reanalysis data. PSY4 hindcasts included vertical temperature profiles, sea surface salinity, and relative water velocity from PSY4 sea ice drift at 0.5 m depth. The reanalysis output is from ERA5 and includes values of atmospheric pressure, temperature, total column water vapor, and wind field velocity (Copernicus Climate Change Service (C3S), 2017).

We use sea ice concentration data on a 6.25 km grid obtained from the 89 GHz channels of the AMSR2 satellite radiometer (Melsheimer & Spreen, 2019; Spreen et al., 2008) to calculate sea ice area *IceA* (ice concentration multiplied by grid cell area and summing up all grid cells within a given region). To calculate sea ice area fluxes *IceIn* and *IceOut* of our study region, the sea ice drift data set from OSI SAF "OSI-405-c: Sea Ice Motion Maps with 48 hours span, on 62.5 km Polar Stereographic Grid" is utilized (Lavergne et al., 2010). Year-round sea ice drift is obtained from a multisensor analysis of SSMIS (91 GHz H&V pol.), ASCAT (C-band backscatter), and AMSR-2 (18.7 and 36.5 GHz) channels. *IceIn* and *IceOut* are calculated by

Table 1
Data Sets Collected During the N-ICE2015 Expedition (Granskog et al., 2018) and Used in This Study

Data		References
(a)	Wind speed, precipitation, air temperature, and specific humidity	Cohen et al. (2017) and Hudson et al. (2015)
(b)	Incident surface shortwave and longwave radiation	Hudson et al. (2016) Taskjelle et al. (2016)
(c)	Sensible and latent heat fluxes from eddy-covariance system deployed on the ice floes	Walden, Hudson, et al. (2017) and Walden, Murphy, et al. (2017)
(d)	Ice core physics-sea ice temperature and salinity	Gerland et al. (2017)
(e)	Snow and ice thickness, snow, ice, and sea surface temperature from IMB data (SIMBA-2015a, c, d and f)	P. Itkin et al. (2015)
(f)	Ice and snow thickness from EM31 and drillings	Rösel et al. (2016) and Rösel and King (2017)
(g)	Sea surface current velocity, temperature, salinity, and heat fluxes from two loosely tethered free-fall microstructure profilers (MSS-90)	Meyer et al. (2016) and Meyer, Sundfjord, et al. (2017)
(h)	Sea surface current velocity, temperature, salinity, and heat fluxes from a turbulence instrument cluster deployed under the ice floes	Peterson et al. (2016, 2017)

Note. The listed references include information on repositories where data can be found.

multiplying the ice drift with ice concentration and grid cell length and summing them up along the transects confining our study region (the polygon depicted in Figures 1a and 1b, with an area of 20,480 km^2).

We represent the rate of change in sea ice area within a given region by the following equation:

$$LocalChanges = \frac{\Delta IceA}{\Delta t} - IceIn + IceOut, \quad (1)$$

where *IceA* is the ice area in the region (km^2) and $\Delta IceA/\Delta t$ the change in ice area from one day to the next, *IceIn* and *IceOut* are the import and export ice area fluxes into and out of the polygon depicted in Figure 1 (km^2 day^{-1}), and *LocalChanges* (km^2 day^{-1}) may be due to melting, ice growth, and ice deformation.

The ice concentration and drift satellite data were used to estimate daily values for *IceA*, *IceIn*, and *IceOut*, and we then solved for *LocalChanges*. When these changes were negative, it was assumed they were a melting proxy, neglecting the contribution of mechanical deformation. Calculations were carried out from 1 January to 30 September 2015. Sea ice fluxes were estimated across the Lines AB, BC, and CD (Figure 1). Sea ice fluxes across Line AD were assumed negligible as they are facing toward land and no significant fluxes are possible here.

Ice area reduction by ice deformation mainly happens in short, episodic events, for example, by convergence during storms. These might cause some of the short-term variability in our time series. Some short-term variability might also be caused by the uncertainty of the satellite measurements. The uncertainty for the ice concentration and therefore also the ice area of a single AMSR2 6.25 × 6.25 km^2 grid cell varies between 5% and 25% depending on ice concentration (Spreen et al., 2008). Assuming errors that are uncorrelated between cells, this results in an uncertainty of about 150 km^2 for *IceA* in our study region for the daily data set. The satellite ice drift data have very low bias (<100 m) when compared with ice buoy drift. The standard deviation of the difference, however, is about 3 km for the 2 day data set (Lavergne et al., 2010). Supported by the low bias, we again assume Gaussian (i.e., uncorrelated) error statistics using the standard deviation as uncertainty estimate and assuming that on average, two out of the three satellite-based drift observations are available. With this reasoning for our three transects, we estimate an uncertainty of about 300 km^2 for the net ice area inflow *IceIn-IceOut* for the daily data set. Together, this results in an uncertainty of 335 km^2 day^{-1} for the daily *LocalChanges* estimates. This uncertainty is smaller but of the same order of magnitude as our average daily *LocalChanges* estimates of −560 ± 30 km^2 day^{-1} (section 3.1). Thus, some of the day-to-day variability can be associated with the uncertainties of the satellite data. Known biases for the ice area and ice drift data are low, and these uncertainties thus will get reduced when averaged over longer time periods. If we assume uncorrelated ice drift observations every 2 days (i.e., the length of the ice drift estimation data set), we end up with an uncertainty of 26 km^2 day^{-1} (300 km^2/$\sqrt{136}$) for the January to September mean ice area inflow into the region of 555 km^2 day^{-1} (i.e., 550 ± 30 km^2 day^{-1}; section 3.1).

Therefore, longer-term negative *LocalChanges* can be associated with ice melt. We also assume that the thickness of incoming sea ice from the north is equal to that leaving in the SW, which should be a conservative assumption for total melt, given that Nansen Basin sea ice is typically thicker than that found in the marginal ice zone over the SW Yermak Plateau (e.g., Ricker et al., 2017).

Atmospheric reanalysis output, spatially averaged for the area defined by the Points A–D (Figure 1), with a 6-hourly frequency were cross-correlated with the ice melting rates estimated from satellite data. The following atmospheric variables were considered: atmospheric pressure, temperature, wind speed and direction, and the curl (vorticity) and divergence of the wind field. Lead and lag times are relative to noon (UTC time) on the day of the estimated ice melt.

2.3. Modeling

2.3.1. Model Setup

We have used an earlier version of the Los Alamos Sea Ice Model (CICE) supported through the CICE Consortium (https://github.com/CICE-Consortium), based on CICE v5.1, in a one-dimensional (1-D) stand-alone mode (Hunke et al., 2015; Turner et al., 2013). This version resolves physical processes vertically, including several interacting components to simulate ice transport, mechanical ridging, and thermohaline dynamics (Hunke et al., 2015). Only the thermohaline dynamics is used in the 1-D simulations described here. Several papers have described CICE developments included in the version used in our study; for example, Jeffery et al. (2011) tested different ways of simulating the transport of tracers in sea ice, while Turner et al. (2013) described a new parameterization of gravity brine drainage. In a detailed sensitivity analysis, Urrego-Blanco et al. (2016) found that sea ice variables, especially sea ice volume, are mostly sensitive to snow-related parameters. The configuration used in the present study includes mushy-layer thermodynamics (Feltham et al., 2006; Hunke et al., 2015), a Delta-Eddington approach for albedo and shortwave radiation fluxes (Hunke et al., 2015), and the gravity drainage approach described by Turner et al. (2013). It is the same configuration described by Duarte et al. (2017) but without the simulation of biogeochemical processes. Model parameters and their values are listed in Table S1.

We forced CICE 1-D stand-alone simulations with atmospheric and oceanographic time series which, in the present study, include the data sets listed in Table 1 and presented in Figure 2. One of the forcing variables is the mixed layer temperature (equivalent to sea surface temperature in the model), which is calculated via a thermodynamic slab-ocean mixed layer parameterization within the CICE model, using a stability-dependent turbulent flux parameterization that is partially controlled by the model mixed layer depth (MLD) parameter. In our simulations, this MLD parameter was either varying or set to a constant value of 15 m as in Duarte et al. (2017), reflecting the typical range within which wind forcing penetrated and homogenized the surface layer during the N-ICE2015 expedition (Meyer, Fer, et al., 2017). When not set to a constant value, the model MLD parameter was based on a "mixing depth" estimated from the Microstructure Profiler data (Table 1g) as the depth at which the dissipation rate of turbulent kinetic energy falls below a threshold value of 3×10^{-7} W kg^{-1} in each vertical profile of dissipation rate. The threshold value was defined based on the analysis of the dissipation rate distribution during the N-ICE2015 expedition (Meyer, Fer, et al., 2017). Water temperature is also influenced by lateral mixing that is not accounted for in the present model configuration. CICE includes a restoring time parameter used to assimilate measured water temperatures and bring values calculated by the slab-ocean mixed layer parameterization close to observations. In the present study a restoring time scale of 1 day was used, as in Jeffery and Hunke (2014) and Duarte et al. (2017), except when otherwise indicated.

The standard CICE 1-D setup uses a minimum default current velocity of 0.001 m s^{-1} to provide background-level shear between the water and the ice and thereby forcing the ocean heat flux. In the present study, we implemented calculation of shear from ocean velocities measured or simulated at 1 or 0.5 m below the ice-ocean interface to better mimic realistic forcing. The shear calculation was done exactly in the same way as in the dynamical component of CICE (Hunke et al., 2015) and following Duarte et al. (2017).

At the end of each time step, the CICE model checks hydrostatic equilibrium and the presence of a negative freeboard, from snow and ice depths and densities. In the case of a negative freeboard, the ice floe is "flooded," and some snow is replaced with the required thickness of snow ice to restore the hydrostatic equilibrium and bring the ice surface to sea level. The new ice has a porosity of the snow. The salinity of the brine occupying the new formed ice is taken as the sea surface salinity. Once the new ice is formed, the vertical ice

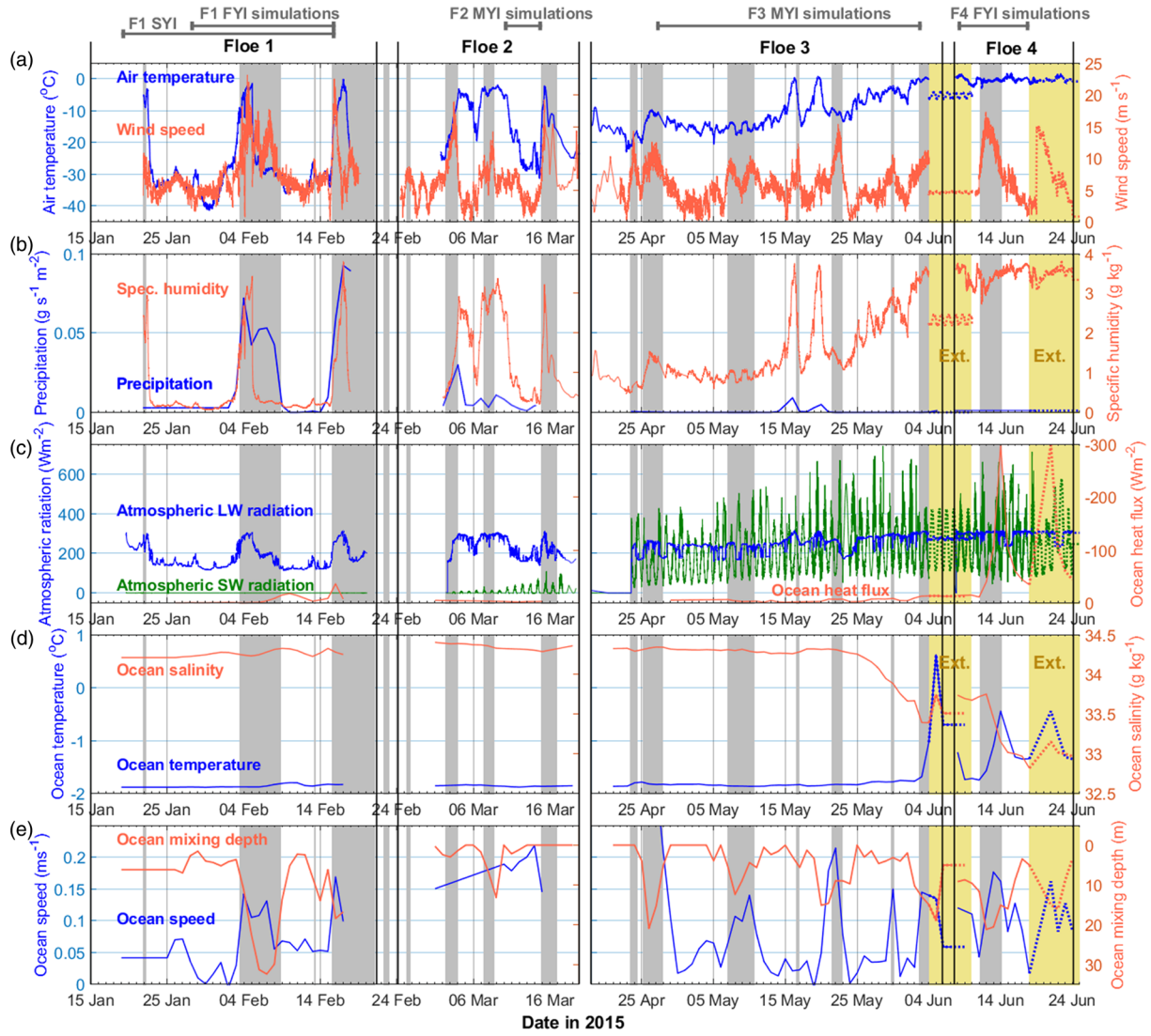

Figure 2. Atmospheric and ocean observations (Table 1) collected during the N-ICE2015 expedition and used to force the CICE model simulations presented in this paper including air temperature, wind speed, specific humidity, precipitation, atmospheric longwave (LW) radiation, atmospheric shortwave (SW) radiation, ocean heat flux, salinity, temperature, mixing depth, and speed. Periods of time during which the data were used to force the CICE simulations (see Table 2 for details) are indicated in gray above subplot (a). Storm periods are shaded gray and show warmer air temperature, high wind speed, significant precipitation, higher LW radiation, deeper ocean mixing depth, and higher ocean speeds. Periods when data were extended for some model simulations (see Table 2 and section 2.3.2) are shaded in yellow and extended data are indicated by dotted lines.

layers are regridded into equal thicknesses while conserving energy and salt (Hunke et al., 2015). During the N-ICE2015 expedition, snow ice was observed in many places (Granskog et al., 2017), but many areas also had negative freeboard without being flooded (Graham et al., 2019; King et al., 2018; Rösel et al., 2017). Therefore, in our CICE model setup, we implemented a simple change in the code allowing us to switch on and off the hydrostatic equilibrium check and snow-ice formation, depending on the ice floes being simulated.

2.3.2. Model Simulations

Model simulations of first year ice (FYI), second year ice (SYI), and multiyear ice (MYI) sites were carried out. The simulations utilized observations listed in Table 1 (see Figure 2) and covered the whole drifting period of the N-ICE2015 expedition in the area north of Svalbard (Figure 1b). Simulations are listed in Table 2, and those named "Standard simulations" correspond to periods when IMB buoy data (Jackson et al., 2013), with sea ice and snow temperatures with high temporal (6 hr) and vertical resolution (2 cm), were available

Table 2
Main Model Simulations

Model simulations		Description
Standard simulations used for model validation and energy budgets	F1_SYI_1, 2, and 3	Floe 1 SYI ice simulated between 19/01/ 2015 and 16/02/2015
	F1_FYI_1, 2, and 3	Floe 1 FYI ice simulated between 28/01/2015 and 16/02/2015
	F2_MYI_1, 2, and 3	Floe 2 MYI ice simulated between 10/03/2015 and 15/03/2015
	F3_MYI_1, 2, and 3	Floe 3 MYI ice simulated between 27/04/2015 and 03/06/2015 and then extended until 10/06/2015, for F3_MYI_1 only, following criteria explained in section 2 and in Supporting Information
Simulations used only for energy budgets	F4_FYI_1 and 2	Floe 4 FYI ice simulated between 08/06/2015 and 18/06/2015 and then extended by a week, for F4_FYI_1 only, following criteria explained in section 2 and in Supporting Information
Simulations used for hypothetical scenarios	F1_YERMAK_SYI_1 and 2	Floe 1 SYI ice simulated between 19/01/2015 and 17/02/2015 with simulated Yermak Plateau oceanographic conditions
	F1_YERMAK_FYI_1 and 2	Floe 1 FYI ice simulated between 28/01/2015 and 17/02/2015 with simulated Yermak Plateau oceanographic conditions
	F3_YERMAK_MYI_1 and 2	Floe 3 MYI ice simulated between 28/01/2015 and 17/02/2015 with simulated Yermak Plateau oceanographic conditions
	F1_SYI_2_AW	Floe 1 SYI on AW with above freezing temperatures (1°C, 3°C, and 5°C) but a winter atmosphere

Note. F1–F4 correspond to the ice floes being simulated (refer Figure 2). FYI, SYI, and MYI stand for first, second, and multiyear ice, respectively. Numbers 1 and 2 contrast simulations without and with hydrostatic equilibrium, respectively. Numbers 1 and 3 contrast simulations with or without a constant mixing layer depth, respectively. Both correspond to simulations without hydrostatic equilibrium. The only exceptions to these rules are Simulations F1_FYI_1 and F1_FYI_3, where hydrostatic equilibrium was switched on at the beginning of the last simulated day to allow ice inundation when it was detected in the observational data (Provost et al., 2017) (refer text).

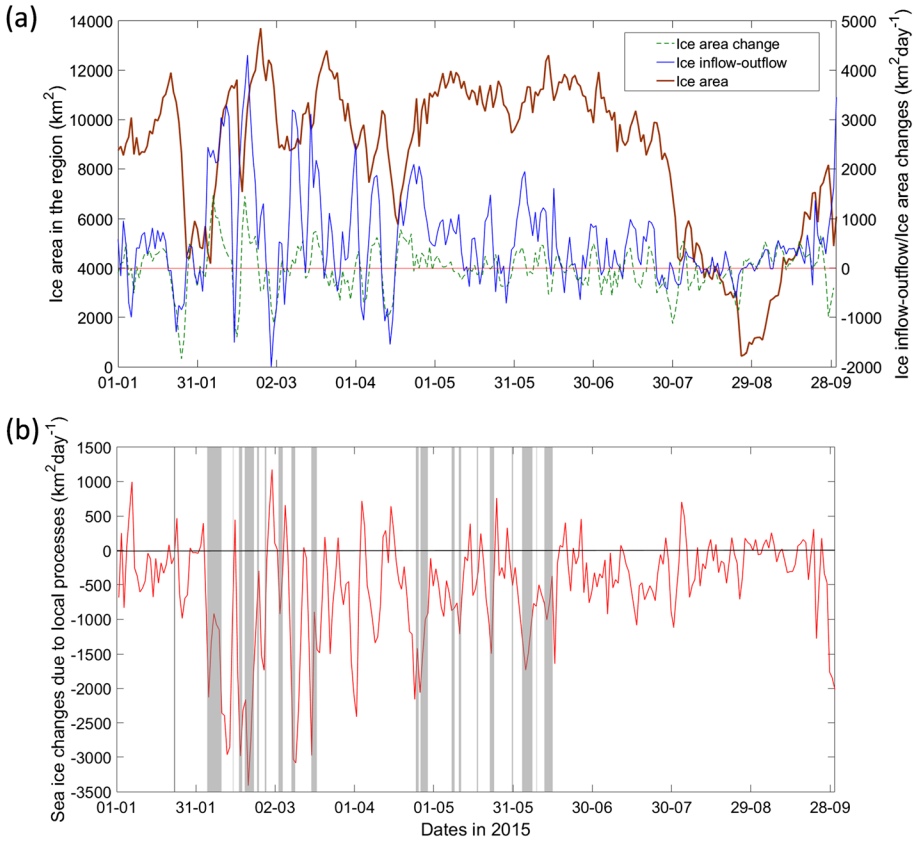

Figure 3. (a) Total ice area (*IceA*, left *y* axis, and Equation 1), ice inflow-outflow (*IceIn-IceOut*, right *y* axis, and Equation 1), and area changes ($\Delta IceA/\Delta t$, right *y* axis, and Equation 1), obtained from satellite data, between 1 January and 30 September 2015 in the area defined by Points A–D in Figure 1. (b) Sea ice changes (*LocalChanges*, Equation 1) for the same area calculated with Equation 1. Negative values are a proxy for melting. Shaded areas show storm periods observed during the N-ICE2015 expedition and described in Cohen et al. (2017).

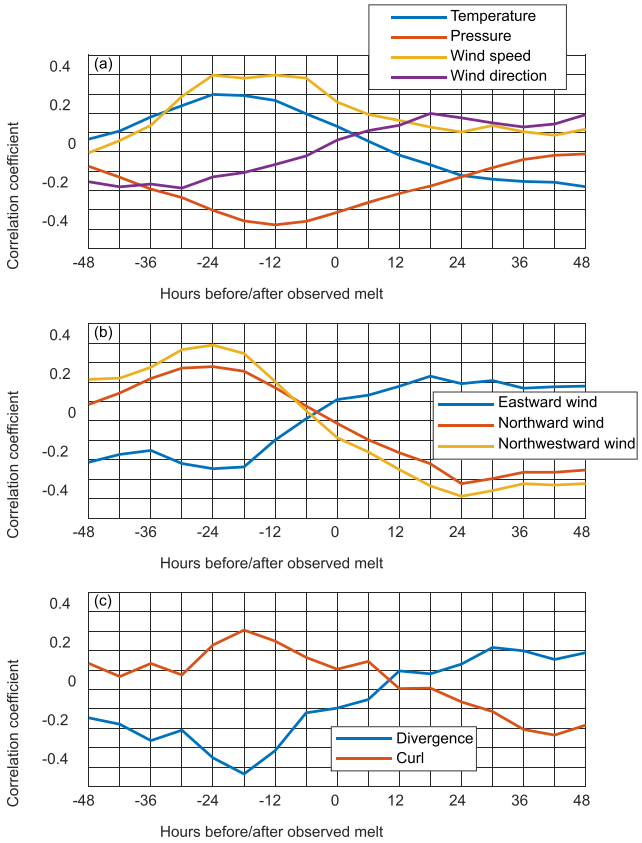

Figure 4. Cross-correlations between melting rates (*LocalChanges*, Equation 1) and (a) air temperature, pressure, wind speed, and wind direction; (b) eastward, northward, and northwestward wind speed; and (c) wind divergence and curl.

(Floes 1–3). Simulations for Floes 3 and 4 (F3_MYI_1, F3_MYI_3, F4_FYI_1, and F4_FYI_2) were extended by a few days (Table 2) to predict the fate of sea ice in periods of enhanced melting. Moreover, simulations were run for hypothetical scenarios attempting to disentangle the role of the hydrographic and atmospheric conditions over and across the Yermak Plateau on sea ice melting (Table 2). Details about these simulations and model parameters and evaluation are given in Supporting Information, including their initial conditions (Tables S1–S6 and Texts S2 and S3).

A time step of 450 s was used in all simulations. Tests conducted with shorter time steps led to similar results. Fifteen ice layers and one snow layer were used in all simulations. Sea ice and snow initial conditions were set to match observations of ice and snow thickness, salinity, and temperature from available data (Text S2 and Tables S3–S6).

3. Results

We first present results based on satellite observations showing that there is large net melting of sea ice imported into the study area north of Svalbard (section 3.1). We then present results from correlations between atmospheric reanalysis data and inferred melt rates (section 3.2). In section 3.3, we present model results.

3.1. Sea Ice Import and Estimated Melting Based on Satellite Data

There is a large net import of sea ice to the area north of Svalbard. The area defined by Points A–D in Figure 1 is about 20,480 km^2, and during spring 2015, it had a mean ice concentration between about 30% and 60% (sea ice area ~6,000–13,000 km^2; Figure 3a), which dropped close to zero in August. The mean net ice import (inflow-outflow) to this area between January and September 2015 was 550 ± 30 km^2 day^{-1}, with substantial variability (Figure 3a; for uncertainty estimates, see section 2.2). This large net import of sea ice would have filled the area entirely within ~37 days, so, clearly, effective melting of sea ice is ongoing in the area. The estimated mean areal melting for the studied area is -560 ± 30 km^2 day^{-1} (Figure 3b), slightly larger than, but within the uncertainty of, the mean net import. This larger mean melting than net import can explain the net loss of ice area between winter and summer (Figure 3a). Winter melting (calculated for January–March) is 810 ± 50 km^2 day^{-1}. Net relative melting of sea ice (obtained by dividing local sea ice area changes [*LocalChanges*] by the ice-covered area [*IceA*], see Equation 1) is 6% day^{-1} between January and September and 9% day^{-1} between January and March. Therefore, higher absolute and relative melt rates are found during winter (January–March), when there is no solar radiation and air temperatures are below zero (Figure 2) (Onarheim et al., 2014; Walczowski & Piechura, 2011).

3.2. Atmospheric Reanalysis and Melting Rates

The highest correlations between atmospheric reanalysis data and melting rates proxy (*LocalChanges*; see Equation 1—when these changes were negative, it was assumed they were a melting proxy, neglecting the contribution of mechanical deformation) for the polygon shown in Figure 1 were negative correlations with wind divergence 18 hr before the melt, positive correlations with wind speed 12 and 24 hr before the melt, and positive correlations with northwestward wind 24 hr before the melt (Figures 4 and S1). This lag of 12 hr indicates that strong winds at 00:00 UTC are correlated with large melt rates during the UTC calendar day beginning at that time.

However, when looking separately at the eastward and northward wind components, the former is negatively correlated with melt, while the latter is positively correlated. Both reverse sign when looking at the

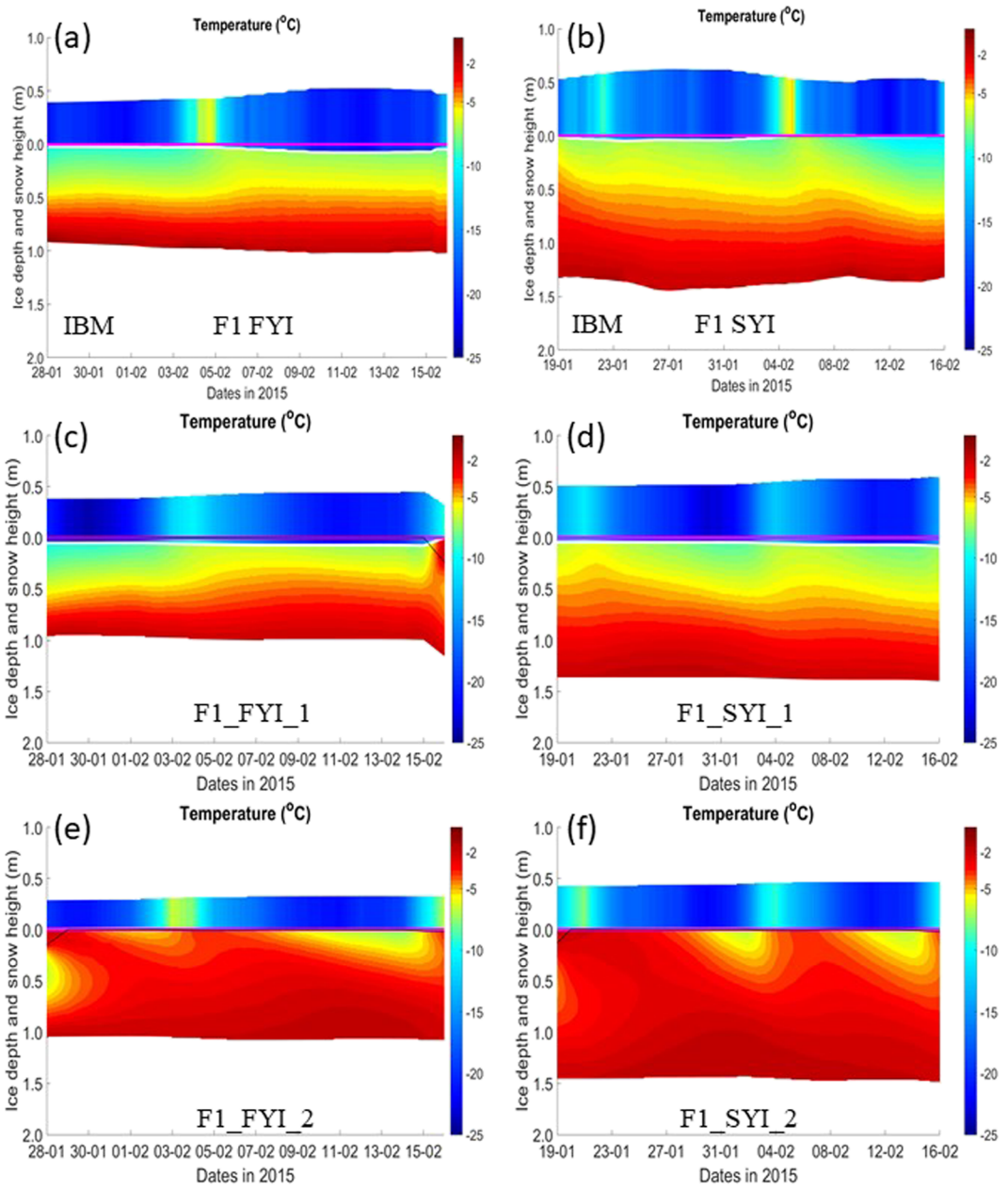

Figure 5. Observed (data from P. Itkin et al., 2015) and modeled sea ice and snow thicknesses and temperatures in Floe 1. Ice temperatures are vertically resolved, whereas snow temperatures are vertically averaged. White and magenta lines show the ice-snow interface and the sea level, respectively. (a, b) Observed results for the IMB buoys, for FYI and SYI, respectively. (c, d) Model results for Simulations F1_FYI_1 and F1_SYI_1 respectively. (e, f) Model results for Simulations F1_FYI_2 and F1_SYI_2, respectively. The thin black line in (c) shows snow ice thickness lower limit. See Table 2 and text for details about model simulations and Figure 2 for forcing data.

winds 12–24 hr after the melt. Looking at all possible wind components, the best correlation was with the strength of wind blowing to 315° (i.e., from the southeast; referred to as "Northwestward wind" in the figures). There are also relatively strong correlations with the divergence of the wind field (negatively correlated) and with the vertical component of the curl of the wind field (positively correlated) (Figures 4 and S1). All correlation coefficients were less than <0.5, corresponding to r^2 values < 0.25 and implying that the percentage of variance of melting rates explained by the correlations was <25% (Figure S1).

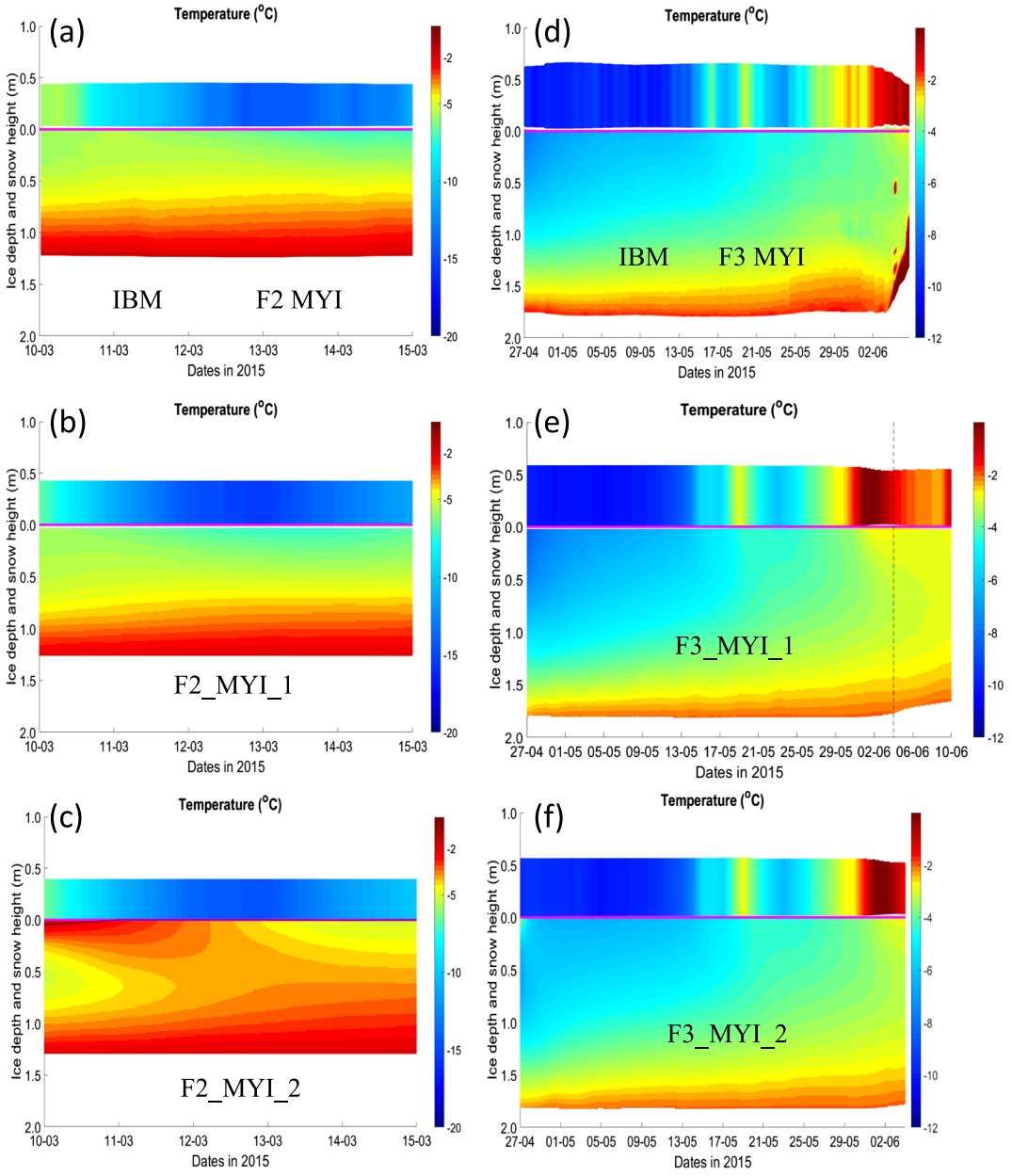

Figure 6. Observed (data from P. Itkin et al., 2015) and modeled sea ice and snow thicknesses and temperatures in Floes 2 (left panels) and 3 (right panels). Ice temperatures are vertically resolved, whereas snow temperatures are vertically averaged. White and magenta lines show the ice-snow interface and the sea level, respectively. (a) Observed results for the IMB buoy, for MYI in Floe 2. (b, c) Model results for Floe 2 Simulations F2_MYI_1 and F2_MYI_2, respectively. (d) Observed results for the IMB buoy, for MYI in Floe 3. (e, f) Model results for Floe 3 Simulations F3_MYI_1 and F3_MYI_2, respectively. Extended period from 4 June only shown for the former simulation, indicated in (e) by the dashed line. See Table 2 and text for details about model simulations and Figure 2 for forcing data.

3.3. Simulated Ice Growth and Melting

3.3.1. Model Evaluation

The simulations used for model validation (standard simulations; Table 2) were those for which IMB buoy data are available (Figures 5 and 6). We ran these simulations without hydrostatic equilibrium or snow-ice formation because the IMB buoy data were obtained in parts of the ice floes with negative freeboard due to the large snow load but where flooding and snow-ice were not observed. There was one exception, and this was Floe 1 simulations for FYI, where we switched on hydrostatic equilibrium on the last simulated day to

Table 3
Model Performance Regarding Vertically Resolved Sea Ice Temperature, for the Standard Simulations Synthesized in Table 2, According to Criteria Synthesized in Allen et al. (2007): the Nash Sutcliffe Model Efficiency (ME) (Nash & Sutcliffe, 1970), the Absolute Value of the Percentage Model Bias |Pbias|, the Cost Function (CF) (OSPAR Commission, 1998), the Root-Mean-Square Error (RMSE), and the r^2

Simulations	ME	|Pbias|	CF	RMSE	r^2
F1_SYI_1	Excellent 0.76	Very good 14.81	Very good 0.40	0.91	0.93
F1_SYI_3	Excellent 0.76	Very good 14.86	Very good 0.40	0.91	0.93
F1_FYI_1	Excellent 0.72	Very good 16.36	Very good 0.51	0.91	0.98
F1_FYI_3	Excellent 0.73	Very good 16.33	Very good 0.50	0.91	0.98
F2_MYI_1	Excellent 0.98	Excellent 3.19	Very good 0.12	0.17	0.99
F2_MYI_3	Excellent 0.98	Excellent 3.22	Very good 0.12	0.17	0.99
F3_MYI_1	Excellent 0.97	Excellent 4.04	Very good 0.14	0.22	0.98
F3_MYI_3	Excellent 0.97	Excellent 3.84	Very good 0.13	0.22	0.98

Note. Quality levels for the first three parameters are based on data presented in Table S1 following Maréchal (2004) and Radach and Moll (2006). All values are dimensionless except the RMSE that is given in the same units of the variables shown in the second column.

allow ice inundation when it was detected in the observational data (Provost et al., 2017). We also ran simulations with the hydrostatic equilibrium switched on for comparative purposes. We compared sensible and latent heat exchanges between the sea ice or snow and the atmosphere with fluxes calculated from an eddy-covariance system (Walden, Murphy, et al., 2017; Walden, Hudson, et al., 2017). Preliminary simulations showed a significant model bias when using the CICE default daily atmospheric forcing frequency (6-hourly for longwave and shortwave radiation). This bias was significantly reduced by increasing it to 1 min frequency, making full usage of available forcing data (Figure S2). Since the model time step is 450 s, the high-frequency forcing time series was in fact used with the time step frequency of 7.5 min, in the simulations listed in Table 2. Shorter time steps led to similar results. All simulations show a performance between "good" and "excellent" according to the criteria employed, when comparing observed (IBM buoy data) and modeled vertically resolved sea ice temperature and vertically averaged snow temperature (Tables 3, 4, and S7 for model quality criteria). This is consistent with similar validation tests described in Duarte et al. (2017) for Floe 3. Simulations with a MLD that was either constant (15 m) or variable (not shown) had a comparable performance and very similar results. Observed and simulated sea ice temperature and ice and snow thickness confirm the good model performance mentioned above, with very similar sea ice temperature gradients; compare Figures 5a and 5c, 5b and 5d, 6a and 6b, and 6d and 6e. Given the similarity (not shown) of the results obtained with fixed and with variable MLD, we will mostly discuss the former.

3.3.2. Scenario Analysis

Comparing Figures 5a, 5b, and 6a with corresponding model results, where hydrostatic equilibrium was switched on—Figures 5e, 5f and 6c, respectively—a positive model bias for ice thickness and a negative bias for snow thickness result from the reestablishment of the hydrostatic equilibrium and snow-ice formation.

Table 4
Model Performance Regarding Vertically Averaged Snow Temperature, for the Standard Simulations Synthesized in Table 2, According to Criteria Synthesized in Allen et al. (2007): the Nash Sutcliffe Model Efficiency (ME) (Nash & Sutcliffe, 1970), the Absolute Value of the Percentage Model Bias |Pbias|, the Cost Function (CF) (OSPAR Commission, 1998), the Root-Mean-Square Error (RMSE), and the r^2

Simulations	ME	|Pbias|	CF	RMSE	r^2
F1_SYI_1	Very good 0.56	Very good 12.24	Very good 0.53	2.45	0.73
F1_SYI_3	Very good 0.56	Very good 12.23	Very good 0.53	2.45	0.73
F1_FYI_1	Excellent 0.86	Excellent 6.64	Very good 0.28	1.54	0.89
F1_FYI_3	Excellent 0.86	Excellent 6.64	Very good 0.28	1.54	0.89
F2_MYI_1	Good 0.45	Very good 11.36	Very good 0.52	1.67	0.76
F2_MYI_3	Good 0.45	Very good 11.37	Very good 0.52	1.67	0.76
F3_MYI_1	Excellent 0.95	Excellent 7.88	Very good 0.16	0.71	0.97
F3_MYI_3	Excellent 0.95	Excellent 7.86	Very good 0.16	0.71	0.97

Note. Quality levels for the first three parameters are based on data presented in Table S1 following Maréchal (2004) and Radach and Moll (2006). All values are dimensionless except the RMSE that is given in the same units of the variables shown in the second column.

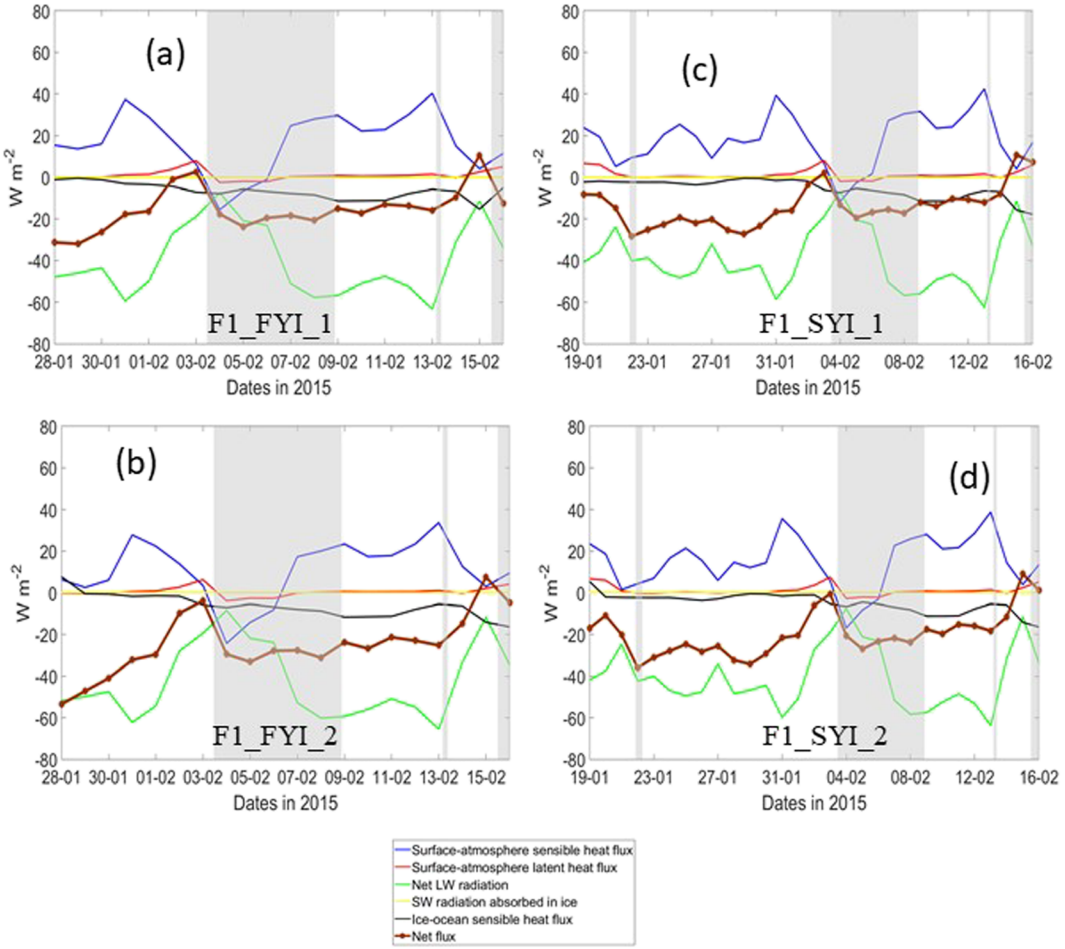

Figure 7. Model daily-averaged energy fluxes (negative fluxes are upward following CICE convention) in Floe 1. (a, b) FYI Simulations F1_FYI_1 and F1_FYI_2, respectively. (c, d) SYI Simulations F1_SYI_1 and F1_SYI_2, respectively. Shaded areas show duration of storm events defined in Cohen et al. (2017). See Table 2 and text for details about model simulations and Figure 2 for forcing data.

This bias was not observed in Floe 3 (cf. Figures 6d and 6f) where the larger ice thickness prevented a negative freeboard for a similar snow load as that of Floe 1. Results for Floe 4 with (Figure S3) and without (not shown) hydrostatic equilibrium were also similar due to the relatively low snow load.

The energy budgets without and with hydrostatic equilibrium (Figures 7a, 7c, 8a, and 8d vs. Figures 7b, 7d, 8c, and 8f, respectively) usually have a very similar behavior with respect to all fluxes involved, with a few exceptions. The most noticeable difference between the two simulations is the more negative energy budget of the latter due to slightly lower sensible heat fluxes from the atmosphere to the surface, driven by the higher sea ice temperatures resulting from the initial flooding, reestablishing the hydrostatic equilibrium, and subsequent latent heat release. One common feature in all energy budgets is the symmetry between sensible heat gains and longwave losses. These fluxes are also the largest ones, except toward the spring/summer, when shortwave radiation may become dominant (Figures 8d, 8f, and S3) and/or toward areas with AW closer to the surface (the case of Floe 4) when ocean heat fluxes may reach >200 W m^{-2} (Figure S3).

Storms lead to rapid changes in all energy fluxes. These changes include (i) a reduction of the net longwave cooling; (ii) a reduction in the sensible heat gain from the atmosphere, leading in some cases to a sensible heat loss; (iii) an increase in latent heat gains by the snow and ice; (iv) an increase in the net energy flow to the ice and a corresponding warming; and (v) effective bottom melting due to increased ocean heat fluxes (Figures 7 and 8). These changes may revert their sign before the storm ends.

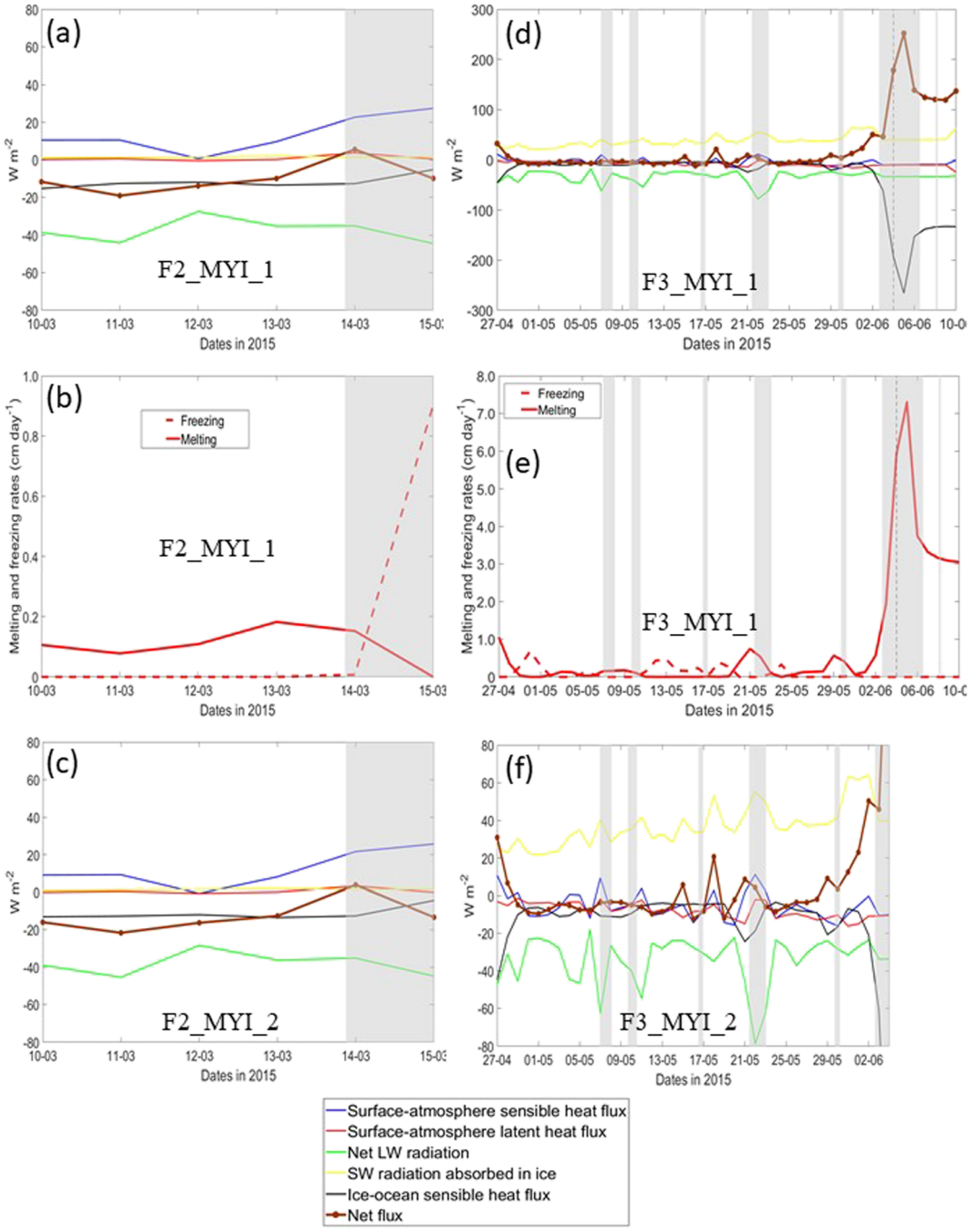

Figure 8. Model daily-averaged energy fluxes (negative fluxes are upward following CICE convention) and freezing and melting rates in Floes 2 (left panels) and 3 (right panels). (a, b) Energy fluxes and freezing and melting rates, respectively, in Simulation F2_MYI_1. (c) Energy fluxes in Simulation F2_MYI_2. (d, e) Energy fluxes and freezing and melting rates, respectively, in Simulation F3_MYI_1. (f) Energy fluxes in Simulation F3_MYI_2. Extended period from 4 June only shown for the F3_MYI_1, indicated in (d) and (e) by the dashed line. Shaded areas show duration of storm events defined in Cohen et al. (2017). See Table 2 and text for details about model simulations and Figure 2 for forcing data.

Switching between Yermak Plateau and deep basin conditions has a significant impact on melt, but the melt during Floe 4 still stands out. Note that our simulations follow each ice floe in a Lagrangian way and that the ocean currents are generally perpendicular, so each flow is constantly exposed to forced mixed layer properties, independent from previous melting. Average freezing rates had maximum values of ~1 mm day^{-1}.

Table 5
Mean Basal Melting and Freezing Rates for Contrasting Simulations Carried Out With Winter Atmospheric Forcing for Floe 1 and Oceanic Forcing for Floe 1 or for the Yermak Plateau (refer to Table 1 for Model Simulations)

Model simulations	Basal melting rates (cm day^{-1})	Freezing rates (cm day^{-1})
F1_SYI_1	0.123	0.027
F1_YERMAK_SYI_1	0.487	0.005
F1_FYI_1	0.159	0.123
F1_YERMAK_FYI_1	0.498	0.022
F3_MYI_1	0.365	0.107
F3_YERMAK_MYI_1	0.524	0.015
F4_FYI_1	3.036	0.103

Note. For reference, results for the summer simulation (Floe 4) are also shown.

Average melting rates were generally 1 order of magnitude higher (Table 5). In the winter simulations of Floe 1, where local hydrographic conditions were replaced by those expected for the Yermak Plateau (F1_YERMAK_SYI_1 and F1_YERMAK_FYI_1; Figure S4), there was up to a threefold increase in the melting rates (Table 5). However, average melt remained on the order of a few mm day^{-1}, well below 3 cm day^{-1} for Floe 4 summer simulation of FYI (F4_FYI_1) (Table 5 and Figure S3). Daily freezing and melting rates became smaller and larger, respectively, with the Yermak hydrographic conditions, and storm periods coincided with peaks in melting rates (Figure 9). Ice temperature patterns remained very similar to those of the standard simulations. In the simulation with Floe 3 placed in wintertime and with Yermak plateau hydrography (F3_YERMAK_MYI_1), there was a considerable cooling of the sea ice (Figure S5), in comparison with the standard simulation (F3_MYI_1), as well a decrease/increase in the melting/freezing rates, consistent with the results for Floe 1. Daily melting rates follow a pattern like those of F1_YERMAK_FYI_1 (Figure 9a).

Looking beyond the main observation periods, in the extra week added to the Floe 3 spring MYI simulation (F3_MYI_1), there was a considerable sea ice warming, an increase in the heat transfer from the ocean to the ice by 2 orders of magnitude, correlated with an increase in the net energy budget of the same order of magnitude (~250 W m^{-2}), and an increase in bottom melting from ~0 to ~7 cm day^{-1} (Figures 6e, 8d, and 8e). In the extended period for Floe 4 FYI simulation (F4_FYI_1), the patterns observed were similar to those of the last week of the main observation period, with large ocean heat fluxes heating the ice, resulting in a relatively large and positive net energy flux and melting rates between 7 and 8 cm day^{-1} (Figures S3a–S3c).

To simulate the fate of Floe 1 if it had drifted into warm AW, Simulation F1_SYI_2_AW (Table 2) was carried out assuming values for the AW varying from 1°C to 5°C (Figure 10), showing only results with (1°C, 3°C, and 5°C). Under such conditions, there is rapid ice melting despite the cold winter atmosphere. Energy fluxes are dominated by the ocean heat fluxes with values of several hundred W m^{-2}. The highest values (in the range 600–1,000 W m^{-2}) were obtained during the larger storm period (between 3 and 8 February) and during the simulation with 5°C AW. To put it into context, with an initial sea ice thickness of 1.4 m, fully melting of the floe took more than 30 days with AW temperature at 1°C, 22 days with 3°C AW, and 18 days with 5°C AW.

4. Discussion

4.1. Satellite and Atmospheric Reanalysis Data

The sea ice boundary between the western (ice-covered) and eastern (ice-free) sides of Fram Strait is sharp. Satellite data for the period 1985–2015 (P. Itkin et al., 2014) display the mean percentage of ice-covered days in April, which is frequently the period of maximum sea ice extent in that region (http://www.mosj.no/no/klima/hav/havisutbredelse.html), and show that the northward ice edge tilts toward the east and reaches north of Svalbard, with open water over much of the northwest Svalbard shelf (Figure 1a). Displaying similar data for each month does not change this general pattern (not shown), except for the eastward extension of the ice-free area northwest of Svalbard and the occasional presence of some ice between the Svalbard shores and the ice-free area west of the archipelago. The results obtained from satellite data for the period January–September 2015 show that most of the ice entering the region near the NW corner of Svalbard (the area defined by Points A–D in Figure 1) melts. Moreover, average melting rates are higher during winter than for the whole study period. The open water area observed consistently in this region (Figure 1a), despite the large sea ice import, is most likely due to melting and not the net result of sea ice transport. We did this detailed study only for January–September 2015, but results are consistent with longer-term average sea ice conditions (Figure 1a). Considering that part of this area remains ice-free also in winter and that local winter air temperatures are predominantly negative (Walczowski & Piechura, 2011), our hypothesis is that the winter melting heat source is the relatively warm inflowing AW. Ideally, this analysis should be done with ice volume,

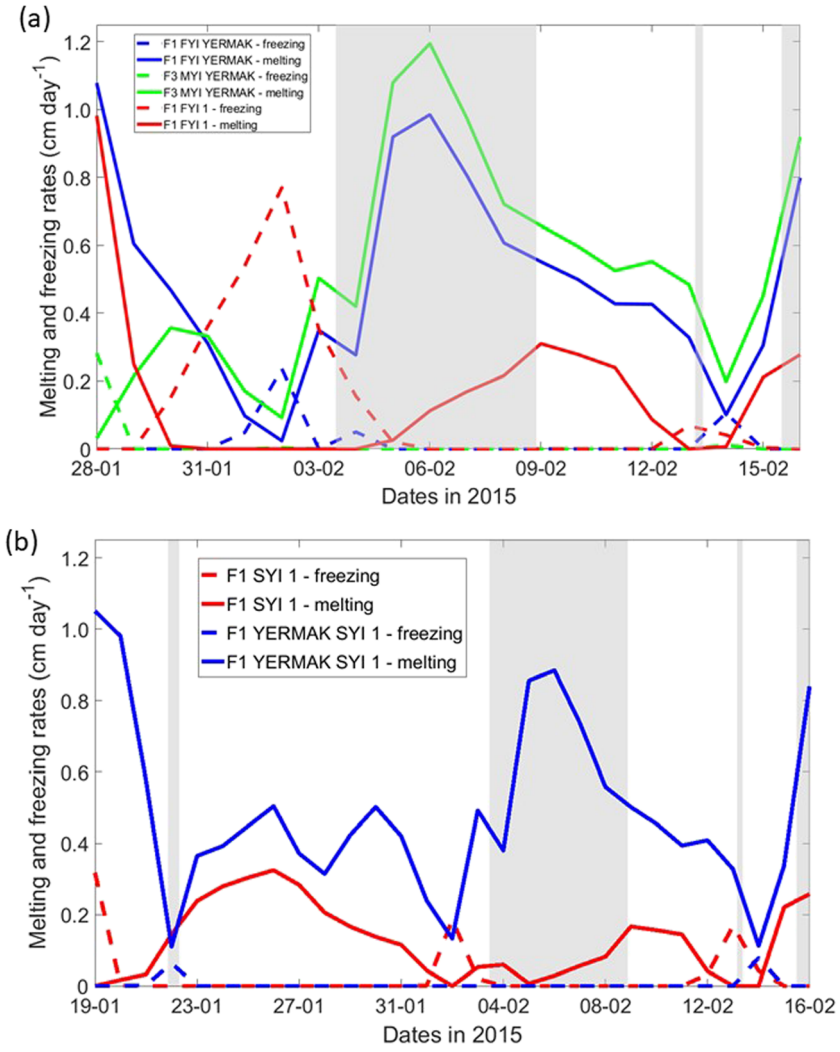

Figure 9. Winter basal melting and freezing rates for standard simulation and for hypothetical scenarios with winter atmospheric forcing and Yermak Plateau oceanographic forcing. Shaded areas show duration of storm events defined in Cohen et al. (2017). See Table 2 and text for details about model simulations and Figure 2 for forcing data.

which is the property that is conserved through thermodynamic and dynamic processes. However, the absence of such data for the surveyed regions with the daily frequency of sea ice concentration and drift data would require interpolating to, at least, weekly time periods for satellite data. Alternatively, climatological data or upscaling of in situ data obtained in limited areas could be used. All these options would limit the accuracy of our estimates. We therefore use *LocalChanges* (Equation 1) as a proxy for the ice melt rate.

Positive time-lagged correlations between wind velocity and melting rates in the surveyed area (Figure 1) suggest that melting is enhanced during and after an increase in the wind speed, especially for winds blowing from the southeast. Negative time-lagged correlations between the divergence of the wind field at the surface and melting rates are consistent with storms enhancing sea ice melt. These results are consistent with observed increases in ocean heat fluxes associated with storms and, especially, when storms and shallow AW are combined (e.g., Graham et al., 2019; Meyer, Fer, et al., 2017; Peterson et al., 2017). However, the correlations also point to a possible influence of sea ice dynamics on our inferred melt rates: Both wind convergence and winds from the southeast (towards the main ice pack) tend to reduce ice area by packing floes together more tightly.

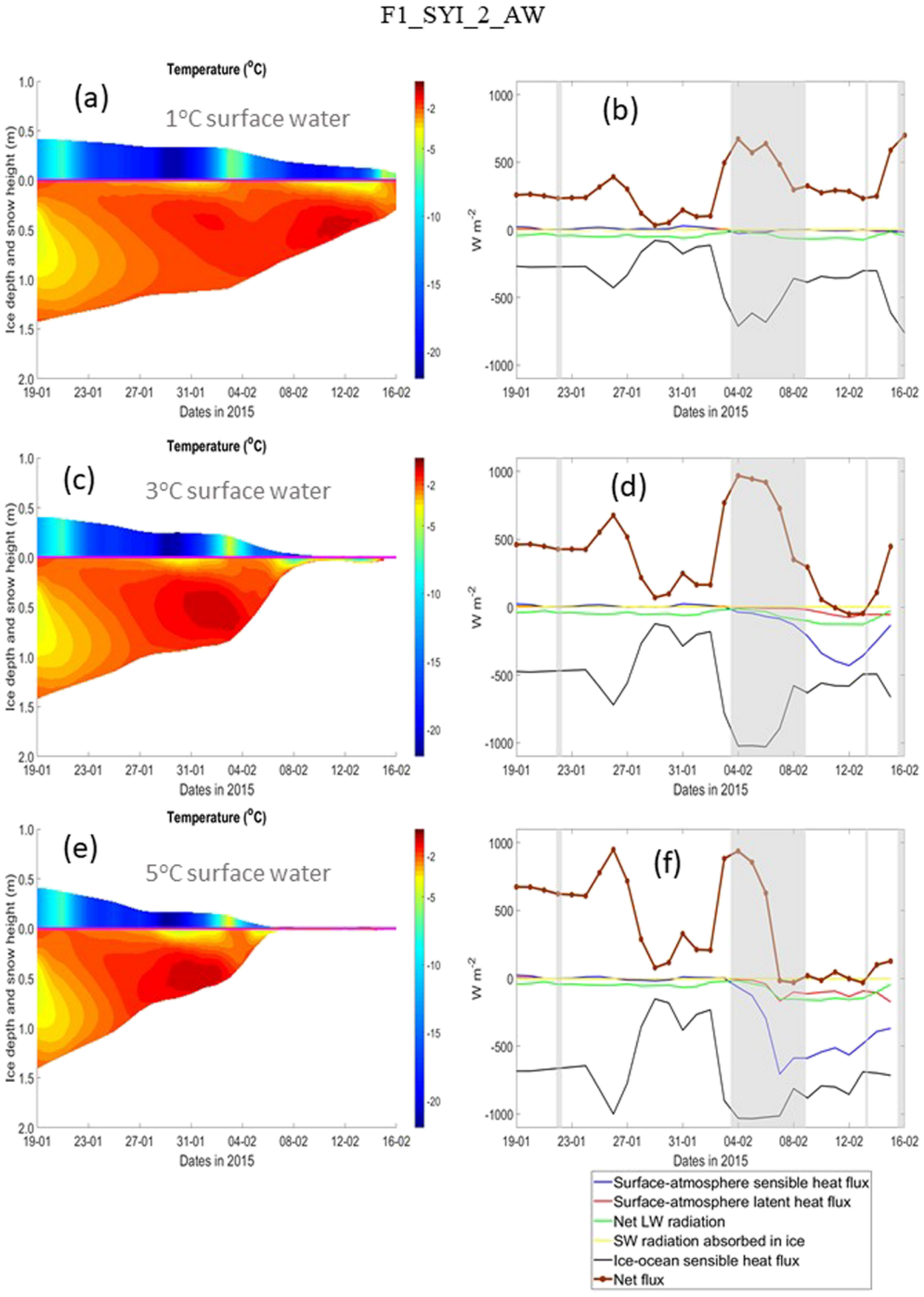

Figure 10. Modeled sea ice and snow thicknesses and temperatures (color maps) and daily-averaged energy fluxes (negative fluxes are upward following CICE convention) for Simulation F1_SYI_2_AW assuming different temperatures for the surface water. (a) and (b) with 1°C; (c) and (d) with 3°C; (e) and (f) with 5°C. In the color maps, only ice temperature is vertically resolved. White and magenta lines show the ice-snow interface and the sea level, respectively. Shaded areas in the energy budget panels show duration of storm events defined in Cohen et al. (2017). See Table 2 and text for details about model simulations and Figure 2 for forcing data.

During the N-ICE2015 expedition, storms were observed during the drift of all ice floes. There are between 20 and 40 extreme cyclone events per winter season, within the area of N-ICE2015 drifts during January–February (81–83.5°N, 16–28°E) (Figure 1b), for the period 1919–2015, with an increasing trend of six events per decade over the same period, according to data from Ny-Ålesund (78.9°N, 11.9°E) in Svalbard (Rinke et al., 2017). Between January and March 2015, six major storm events were observed during the N-ICE2015 expedition (Cohen et al., 2017). These storms fractured the ice cover, enhanced ocean-ice-atmosphere heat fluxes, and made the ice more susceptible to lateral melt (Graham et al., 2019). Moreover, snowfall during storms deepened the snow pack, insulated the sea ice, and inhibited ice growth for the remaining winter season. Despite the significant atmospheric warming observed during winter storms, air temperature remained negative. Storms have been shown to increase ocean heat fluxes roughly twofold in comparison to the background level (Meyer, Fer, et al., 2017). Note however that strong tidal currents around the slopes of the Yermak Plateau lead to increased internal wave activity and can also enhance background mixing rates (Padman et al., 1992). Therefore, we wanted to investigate whether storms are a necessary condition to keep the sharp transition between open and ice-covered waters observed along the NW Svalbard shores.

4.2. Modeling

4.2.1. Model Performance

Before linking model results with the topics discussed above, the model performance is discussed to evaluate the reliability of model results obtained for the nonvalidation scenarios (Table 2).

Using lower (daily) or higher (minute) frequency atmospheric forcing did not have a significant effect on model performance regarding sea ice and snow thickness and sea ice temperature, which were similar in both cases (not shown). However, modeled sensible heat flux was clearly biased with the daily frequency forcing (Figures S2a vs. S2b), exhibiting wider variations between negative (from the ice) and positive (to the ice) fluxes. Larger variations in sensible heat fluxes were "compensated" by opposite variations of latent heat and longwave fluxes (not shown) because, as soon as surface snow temperature is affected by an increased sensible heat flux, the temperature change stimulates an opposite response by the other fluxes. Therefore, the physical feedbacks stabilize the system, reducing the bias in net energy fluxes and thereafter in calculated ice temperatures. The following equations, taken from Hunke et al. (2015) and used in the CICE model, illustrate these physical feedbacks. The sensible (F_s), latent (F_l), and outgoing (from the ice and snow to the atmosphere) longwave (F_L) fluxes are calculated with

$$F_s = C_s(\theta_a - Tsf) \tag{2}$$

$$F_l = C_l(Q_a - Qsf) \tag{3}$$

$$F_L\uparrow = \varepsilon\sigma(Tsf)^4 \tag{4}$$

where C_s and C_l are nonlinear heat transfer coefficients described in Hunke et al. (2015); θ_a is the potential air temperature in Kelvin; Tsf is the surface temperature of snow or ice in Kelvin; Q_a and Q_{sf} are the air and the surface saturation specific humidity, respectively; $\varepsilon = 0.95$ is the emissivity of snow or ice; and σ is the Stefan-Boltzmann constant. Qsf is calculated with

$$Qsf = (q_1/p_a)\exp(-q_2/Tsf) \tag{5}$$

where q_1 and q_2 are constants and ρ_a is surface air density.

The feedbacks between Equations 2 and 4 are straightforward: Any gains in sensible heat leading to an increase in Tsf will lead to an increase in outgoing longwave fluxes, counteracting the temperature increase. The feedbacks between Equations 2 and 3 act through changes in Qsf (Equation 5) which increases with Tsf. Therefore, any increase in Tsf, everything else being equal, will lead to a negative change in latent fluxes.

The root of the problem with the sensible heat flux bias is not physical but numerical. The lower the frequency forcing we use, the longer the model will "assume" something about the state of variables driving the fluxes, such as air temperature, in the case of sensible heat fluxes. We were not able to explore more in depth these details due to lack of data on some of the fluxes. The use of minute-frequency atmospheric forcing significantly improved the calculation of sensible heat fluxes and brought latent heat fluxes to

values of the same magnitude as those estimated by Walden, Hudson, et al. (2017) and Walden, Murphy, et al. (2017) (typically between ±20 W m^{-2}). Moreover, according to the various criteria employed, model performance was between good and excellent for all the simulations that could be compared with empirical data, covering Floes 1–3. Therefore, it seems reasonable to assume that model results are reliable for the non-validation scenarios, and these will be further discussed below.

4.2.2. Flooding and Snow-Ice Formation

Despite the widespread negative freeboard during N-ICE2015 (Graham et al., 2019; King et al., 2018), situations where flooding and snow-ice formation did not take place were common. This suggests that snow ice forms predominantly around the floe edges and when dynamics drive cracking or when the ice warms enough to become permeable. The major part of the floe would thus not feel the negative freeboard. This is likely to happen in relatively large ice floes; the size of floes studied during N-ICE2015 was typically >1 km. This situation implies that local imbalances in hydrostatic equilibrium at the floe level were compensated by some horizontal floe deformation and/or snow-ice accumulation in other areas of the floe. Good model performance depended on switching off hydrostatic equilibrium for Floes 1 and 2, because using the default CICE configuration leads to a rapid decrease in snow thickness at the expense of snow-ice formation (Figures 5c and 5d vs 5e and 5f and Figures 6b vs. 6c). The cumulative effect of winter storms led to a snow depth of ~50 cm—higher than the climatological mean (<40 cm) (Graham et al., 2019; Warren et al., 1999). Its insulating effect inhibited thermodynamic ice growth in winter/early spring (Floes 1–3) (Graham et al., 2019; Merkouriadi, Cheng, et al., 2020).

4.2.3. Sea Ice Melt Rates

During most of the winter, sensible heat fluxes were positive (toward the ice), resulting from snow skin temperatures being generally lower than air temperatures. This was due to the imbalance between downwelling and upwelling longwave radiation (Walden, Hudson, et al., 2017). The net longwave radiation was negative and cooled the ice because outgoing fluxes were larger than the incoming ones under clear skies (Figures 7a, 7c, 8a, and 8d). However, there were also occurrences of sensible heat loss from the snow to the atmosphere. This happened during Floe 1 due to large and rapid changes during the passage of a cold front during one of the storms, leading to the advection of cold air over the recently warmed snow surface, allowing the atmosphere to cool the surface through turbulent mixing of colder air down to the warmer surface. The early phases of storms led to a transient slightly positive net energy budget and to surface warming (Figure 7). However, none of these changes led to significant melting of the ice or snow (Figure 9 and Table 5). Combining our estimated relative melting rates from satellite data of between 6% and 9% day^{-1} (section 3.1) and the typical range of ice thicknesses (between 1 and 2 m) measured in Floes 1–4 during N-ICE2015 (Rösel et al., 2016, 2017; Rösel & King, 2017) suggests regional melt rates around ~6–9 cm day^{-1} for 1 m thick ice and twice as much for 2 m thick ice. When winter oceanographic conditions of Floe 1 were replaced by those of the Yermak Plateau, the most noticeable change in the energy budgets was increases in ocean heat fluxes from a few W m^{-2} to ~40 W m^{-2}. This was very visible during the storm periods (Figures 7a and 7c vs. Figure S4c and S4g), but there was still only limited melting at the ice bottom (up to 1 cm day^{-1}; Figure 9)—well below the melting rates estimated above. In all our simulations, melting rates of that magnitude (~6–9 cm day^{-1}) were obtained only for Floe 4 (summer) (Figure S3c and Table 5), for the extension of Floe 3 simulation (spring) (Figure 8e) and for the simulations directly over AW (winter) (refer Table 2), with melting rates up to ~20 cm day^{-1} (not shown).

The case of Floe 4 results from a combination of above-freezing air temperatures and ocean heat fluxes of almost 300 W m^{-2}, 1 to 2 orders of magnitude higher than those of all standard simulations (refer Table 2). The high ocean fluxes during Floe 4 drift (Figure 1b), between the Yermak Plateau and the Svalbard shore, resulted from the presence of AW close to the surface (less than 50 m depth in some places) and above-freezing water temperatures below the ice, associated with Warm Polar Surface Water (Figure 4 in Meyer, Sundfjord, et al., 2017), enhanced by the occurrence of a storm.

Floe 3 showed very limited melting until the last part of its drift, when it was already over the Yermak Plateau (Figure 1b) and also during the extended period when environmental conditions reproduced those observed in the last 3 days of the drift (Figures 8d and 8e), with above-freezing water temperatures between −1°C and 0°C. Melting rates reached 7 cm day^{-1}. As for Floe 4, the nearby presence of shallow AW and Warm Polar Surface Water (Meyer, Sundfjord, et al., 2017) explains much of the observed bottom melt as

reflected by the large increase in ocean heat fluxes. However, the occurrence of positive air temperatures prevents the extrapolation of obtained results to a possible winter situation. The absence of significant melting with Floe 1 simulations using Yermak Plateau hydrography from late spring does not provide a straightforward explanation of satellite-derived winter melting rates.

The rationale behind the last scenario (F1_SYI_2_AW in Table 2) was to estimate sea surface temperatures required to obtain winter melting consistent with values calculated from satellite data, possibly leading to ice-free conditions. All tested sea surface temperatures (1°C, 3°C, and 5°C) led to relatively rapid melting, especially for values ≥3°C (Figure 10), when 1.5 m of ice melted completely in less than 20 days. In all three cases, melting was clearly accelerated during the passage of storms. Considering Area ABCD (Figure 1), with a length scale of ~200 km and Floe 4 drift velocity measured during N-ICE2015 (~24 km day^{-1}), a transit time of <10 days is expected. Therefore, the time for complete ice melting in Scenario F1_SYI_2_AW with temperatures ≥3°C is comparable to the above transit time scales, showing that the presence of AW close to the ice is a necessary condition to keep the studied area ice-free in winter. Furthermore, having sea surface temperature ≥5°C leads to maximal net ocean energy fluxes and melting rates prior to a storm comparable to those calculated during the passage of a storm (Figures 10e and 10f). Therefore, while we have shown the importance of storms in enhancing ocean heat fluxes to the ice and increasing melting rates, we also show that once surface waters are warm enough (≥5°C), storms are no longer necessary to keep the ice-free conditions.

The temperature range tested with F1_SYI_2_AW (Table 2) is realistic considering results obtained from transects around 79°N and between 4° and 8.78°E conducted in January, August, and May 2014 near the southern edge of Figure 1b and with upper-ocean temperatures above 6°C in January and August and above 3°C in May (Basedow et al., 2018). Moreover, sea surface temperature values from moorings deployed east of Area ABCD (Figure 1), at 79°N and 31°E, in 2012–2013, reached values between 1°C and 2°C for most of autumn and winter (Renner et al., 2018). Below the upper 20 m, even warmer water was generally observed.

4.2.4. Storms, Transit Times, and Heat Loss

The relatively high frequency of storms in winter makes them a reliable mixing mechanism for providing energy for sea ice melting. Transects conducted in autumn 2001, across the Svalbard Branch of the AW west and north of Spitsbergen, show that AW cools down along this path and is progressively replaced at the surface by colder and less saline water resulting from sea ice melting (Cokelet et al., 2008). We expect that, along the same path, the importance of surface mixing, which can break the density barrier formed by the surface water and thereby deliver ocean heat to drive ice melt, increases; see, also, Figure 2 in Onarheim et al. (2014). This is in line with the idea that, in the Eastern Nansen Basin, increased heat transfer from the AW to the surface mixed layer in winter is enhanced by strong winter storms (Polyakov et al., 2017). According to the same authors, the gradual weakening of stratification and shoaling of the AW eastward facilitates progressively deeper ventilation and heat transfer from the AW toward the surface.

Transit times larger than the ~10 days estimated above provide further support for our arguments. Onarheim et al. (2014) used drift speeds that were lower by 1 order of magnitude for an area along all of the north coast of Svalbard (including our Area ABCD shown in Figure 1) and based on Polar Pathfinder Sea Ice Motion Vectors (NSIDC) (Tschudi et al., 2019). This would alleviate a possible time limitation for ice melting around the NW corner of Svalbard. These authors suggest that residence time above AW is more limiting for sea ice melting than the available heat in surrounding waters.

Heat loss from the upper ocean to the atmosphere and sea ice along the path of the AW north of Svalbard has been estimated to be 520 W m^{-2} (Cokelet et al., 2008). Values measured during the N-ICE2015 expedition, in the ice-ocean boundary layer, were generally lower (Figure 1b), except during storms when they were of similar magnitude (Meyer, Fer, et al., 2017; Peterson et al., 2017). These values compare well with some of the highest estimates we obtained with F1_SYI_2_AW scenario. However, they are lower than the highest model predicted values of ~1,000 W m^{-2}.

5. Summary and Conclusion

There is a general consensus that the delivery of oceanic heat by AW to the area north of Svalbard keeps a substantial part of that region ice-free, even during winter. However, to the best of our knowledge, it has yet to be established quantitatively what temperature and mixing requirements are necessary to melt sea ice fast

enough in realistic winter conditions. We used observations from the N-ICE2015 expedition and the Los Alamos Sea Ice Model (CICE) together with atmospheric reanalysis and remote sensing of sea ice drift and concentration to assess melting of sea ice in this area.

Our main conclusions are that warm near-surface AW is directly responsible for melting in the Whalers Bay area, that most of the sea ice melts within 2 weeks, and that the melting is enhanced by storms. For water temperatures ≥5°C, the ocean is warm enough to keep the region ice-free without the help of storms, thus suggesting that under these conditions, sufficient vertical mixing is available regardless of atmospheric forcing in this area (Meyer, Sundfjord, et al., 2017; Padman et al., 1992). However, the CICE 1-D model simulations ignore lateral ocean heat fluxes, dynamic instabilities, and other relevant processes. Further analysis would be needed to ascertain the relative importance of storms in warmer ocean conditions. Our results suggest that increased winter storm frequency (Rinke et al., 2017), in addition to increased heat content of the AW (Onarheim et al., 2014), has combined to drive additional sea ice loss further eastward in the Eurasian basin (Polyakov et al., 2017).

The satellite-derived time series of sea ice cover from the NW corner of Svalbard indicate strong net melting of sea ice in Whalers Bay, both in summer and winter. During winter, there is a large net import of sea ice to the area (Figure 3), and if no melting had taken place, the area would be fully sea ice covered in about 1 month.

The N-ICE2015 in situ observations of snow and sea ice thickness, internal ice temperature, and atmospheric forcing document that north of Whalers Bay, there is only modest melting and also virtually no winter freezing despite negative air temperatures, due to insulation by the thick snow cover (e.g., Graham et al., 2019; Merkouriadi, Cheng, et al., 2017, 2020; Merkouriadi, Liston, et al., 2020). Strong melting only occurs when sea ice drifts south over near-surface warm AW. Usually AW is flowing below a thin layer of Polar Surface Water, but some of its heat is still transferred to the sea ice, in particular when the passage of atmospheric storms provides increased ocean mixing (Meyer, Fer, et al., 2017). Moreover, strong winds associated with storms fracture the ice and make it more susceptible to lateral melt (Graham et al., 2019).

The CICE 1-D numerical model experiments indicate that ocean heat fluxes of several hundred W m^{-2} are required to attain the satellite-observed melting rates; these fluxes are only realistic when ice drifts over near-surface warm AW. Altogether, the observations and model simulations show that most of the intense sea ice melting north of Svalbard takes place in a narrow band closely following the AW boundary current.

Our modeling results provide strong evidence for good performance of the CICE model under a relatively wide range of atmospheric and ocean forcing, emphasizing the need for high-frequency (hour to minute scale) atmospheric forcing for a proper calculation of ice-atmosphere heat exchanges. The common occurrence of sea ice with a negative freeboard without snow-ice formation poses challenges on how to properly address hydrostatic equilibrium in Pan-Arctic models and prevent the potential for overestimation of ice inundation and snow-ice formation.

The sea ice cover of the Eurasian Basin thus appears directly responsive to AW temperature and depth and winter storm frequency. Understanding present and future changes of ocean and atmospheric forcing and processes driving their variability is key for predicting future sea ice cover north of Svalbard.

Data Availability Statement

Observational data from the N-ICE2015 campaign used in this study are publicly available at the Norwegian Polar Data Centre: https://data.npolar.no/dataset/7f7e56d0-9e70-4363-b37d-17915e09a935 under the keyword N-ICE2015.

References

Allen, J. I., Holt, J. T., Blackford, J., & Proctor, R. (2007). Error quantification of a high-resolution coupled hydrodynamic-ecosystem coastal-ocean model: Part 2. Chlorophyll-a, nutrients and SPM. *Journal of Marine Systems*, *68*(3–4), 381–404. https://doi.org/10.1016/j.jmarsys.2007.01.005

Årthun, M., Eldevik, T., Smedsrud, L. H., Skagseth, O., & Ingvaldsen, R. B. (2012). Quantifying the influence of Atlantic heat on Barents sea ice variability and retreat. *Journal of Climate*, *25*(13), 4736–4743. https://doi.org/10.1175/Jcli-D-11-00466.1

Acknowledgments

This work has been supported by the Norwegian Polar Institutes Centre for Ice, Climate and Ecosystems (ICE), through the N-ICE project; by the Fram Centre Arctic Ocean flagship project "Ecosystem modeling of the Arctic Ocean around Svalbard (ArctisMod)"; by the Research Council of Norway through the Nansen Legacy project (276730); and by the Norwegian Metacenter for Computational Science application "NN9300K - Ecosystem modeling of the Arctic Ocean around Svalbard". A. M. acknowledges support from the ARC Centre of Excellence for Climate Extremes (CE170100023). G. S. was supported by the Deutsche Forschungsgemeinschaft (DFG) (Project 268020496 – TRR 172), within the Transregional Collaborative Research Center "ArctiC Amplification: Climate Relevant Atmospheric and SurfaCe Processes, and Feedback Mechanisms (AC)3." We thank the captains, crews, engineers, and science parties during N-ICE2015 for their help in making this study possible. We thank the U. S. Department of Energy's (DOE) Earth and Environmental System Modeling Program for allowing the use of this version of the CICE model, which includes updated biogeochemistry parameterizations within a "column package" developed as part of the Energy Exascale Earth System Model (E3SM) project. Tuning and model validation work performed under the DOE Regional and Global Modeling and Analysis Program also contributed to these results. A special thanks to Anders Skoglund for helping with Figure 1.

Assur, A. (1958). Composition of sea ice and its tensile strength. In Arctic sea ice; conference held at Easton, Maryland, February 24–27, 1958, Volume 598 of Publs. Natl. Res. Coun. Wash., pp. 106–138, Washington, DC, US.

Basedow, S. L., Sundfjord, A., von Appen, W.-J., Halvorsen, E., Kwasniewski, S., & Reigstad, M. (2018). Seasonal variation in transport of zooplankton into the Arctic Basin through the Atlantic gateway, Fram Strait. *Frontiers in Marine Science*, *5*. https://doi.org/10.3389/fmars.2018.00194

Beszczynska-Möller, A., Fahrbach, E., Schauer, U., & Hansen, E. (2012). Variability in Atlantic water temperature and transport at the entrance to the Arctic Ocean, 1997-2010. *ICES Journal of Marine Science*, *69*(5), 852–863. https://doi.org/10.1093/icesjms/fss056

Carmack, E., Polyakov, I., Padman, L., Fer, I., Hunke, E., Hutchings, J., et al. (2015). Toward quantifying the increasing role of oceanic heat in sea ice loss in the New Arctic. *Bulletin of the American Meteorological Society*, *96*(12), 2079–2105. https://doi.org/10.1175/Bams-D-13-00177.1

Cohen, L., Hudson, S. R., Walden, V. P., Graham, R. M., & Granskog, M. A. (2017). Meteorological conditions in a thinner Arctic sea ice regime from winter to summer during the Norwegian Young Sea ICE expedition (N-ICE2015). *Journal of Geophysical Research: Atmospheres*, *122*, 7235–7259. https://doi.org/10.1002/2016JD026034

Cokelet, E. D., Tervalon, N., & Bellingham, J. G. (2008). Hydrography of the West Spitsbergen Current, Svalbard Branch: Autumn 2001. *Journal of Geophysical Research*, *113*, C01006. https://doi.org/10.1029/2007jc004150

Copernicus Climate Change Service (C3S) (2017). ERA5: Fifth generation of ECMWF atmospheric reanalyzes of the global climate. Copernicus Climate Change Service Climate Data Store (CDS). https://cds.climate.copernicus.eu/cdsapp#!/home

Crews, L., Sundfjord, A., & Hattermann, T. (2019). How the Yermak Pass Branch regulates Atlantic water inflow to the Arctic Ocean. *Journal of Geophysical Research: Oceans*, *124*, 267–280. https://doi.org/10.1029/2018JC014476

Duarte, P., Meyer, A., Olsen, L. M., Kauko, H. M., Assmy, P., Rösel, A., et al. (2017). Sea ice thermohaline dynamics and biogeochemistry in the Arctic Ocean: Empirical and model results. *Journal of Geophysical Research: Biogeosciences*, *122*, 1632–1654. https://doi.org/10.1002/2016JG003660

Feltham, D. L., Untersteiner, N., Wettlaufer, J. S., & Worster, M. G. (2006). Sea ice is a mushy layer. *Geophysical Research Letters*, *33*, L14501. https://doi.org/10.1029/2006gl026290

Gallet, J.-C., Merkouriadi, I., Liston, G. E., Polashenski, C., Hudson, S., Rösel, A., & Gerland, S. (2017). Spring snow conditions on Arctic sea ice north of Svalbard, during the Norwegian Young Sea ICE (N-ICE2015) expedition. *Journal of Geophysical Research: Atmospheres*, *122*, 10,820–10,836. https://doi.org/10.1002/2016JD026035

Gerland, S., Granskog, M.A., King, J., & Rösel, A. (2017). N-ICE2015 ice core physics: Temperature, salinity and density (data set). Norwegian Polar Institute. https://doi.org/10.21334/npolar.2017.c3db82e3

Graham, R. M., Itkin, P., Meyer, A., Sundfjord, A., Spreen, G., Smedsrud, L. H., et al. (2019). Winter storms accelerate the demise of sea ice in the Atlantic sector of the Arctic Ocean. *Scientific Reports*, *9*(1), 9222. https://doi.org/10.1038/S41598-019-45574-5

Granskog, M. A., Fer, I., Rinke, A., & Steen, H. (2018). Atmosphere-ice-ocean-ecosystem processes in a thinner Arctic sea ice regime: The Norwegian Young Sea ICE (N-ICE2015) expedition. *Journal of Geophysical Research: Oceans*, *123*, 1586–1594. https://doi.org/10.1002/2017JC013328

Granskog, M. A., Rosel, A., Dodd, P. A., Divine, D., Gerland, S., Martma, T., & Leng, M. J. (2017). Snow contribution to first-year and second-year Arctic sea ice mass balance north of Svalbard. *Journal of Geophysical Research: Oceans*, *122*, 2539–2549. https://doi.org/10.1002/2016JC012398

Hudson, S. R., Cohen, L., & Walden, V. P. (2015). N-ICE2015 surface meteorology (data set). Norwegian Polar Institute, https://doi.org/10.21334/npolar.2015.056a61d1

Hudson, S. R., Cohen, L., & Walden, V. P. (2016). N-ICE2015 surface broadband radiation data (data set). Norwegian Polar Institute, https://doi.org/10.21334/npolar.2016.a89cb766

Hunke, E. C., Lipscomb, W. H., Turner, A. K., Jeffery, N., & Elliot, S. (2015). CICE: The Los Alamos sea ice model documentation and user's manual version 5.1. Tech. Rep., LA-CC-06-012, Los Alamos National Laboratory, Los Alamos, N. M.

Itkin, M., König, M., Spreen, G., & Vongraven, D. (2014). Arctic sea ice frequency with maximum and minimum extents (data set). Norwegian Polar Institute. https://doi.org/10.21334/npolar.2014.a89b2682

Itkin, P., Spreen, G., Cheng, N., Doble, M., Gerland, S., Granskog, S. J., Helgeland, C. (2015). N-ICE2015 buoy data (data set). Norwegian Polar Institute, https://doi.org/10.21334/npolar.2015.6ed9a8ca

Itkin, P., Spreen, G., Cheng, B., Doble, M., Girard-Ardhuin, F., Haapala, J., et al. (2017). Thin ice and storms: Sea ice deformation from buoy arrays deployed during N-ICE2015. *Journal of Geophysical Research: Oceans*, *122*, 4661–4674. https://doi.org/10.1002/2016JC012403

Jackson, K., Wilkinson, J., Maksym, T., Meldrum, D., Beckers, J., Haas, C., & Mackenzie, D. (2013). A novel and low-cost sea ice mass balance buoy. *Journal of Atmospheric and Oceanic Technology*, *30*(11), 2676–2688. https://doi.org/10.1175/Jtech-D-13-00058.1

Jeffery, N., & Hunke, E. C. (2014). Modeling the winter-spring transition of first-year ice in the western Weddell Sea. *Journal of Geophysical Research: Oceans*, *119*, 5891–5920. https://doi.org/10.1002/2013JC009634

Jeffery, N., Hunke, E. C., & Elliott, S. M. (2011). Modeling the transport of passive tracers in sea ice. *Journal of Geophysical Research*, *116*, C07020. https://doi.org/10.1029/2010jc006527

King, J., Skourup, H., Hvidegaard, S. M., Rösel, A., Gerland, S., Spreen, G., et al. (2018). Comparison of freeboard retrieval and ice thickness calculation from ALS, ASIRAS, and CryoSat-2 in the Norwegian Arctic to field measurements made during the N-ICE2015 expedition. *Journal of Geophysical Research: Oceans*, *123*, 1123–1141. https://doi.org/10.1002/2017JC013233

Koenig, Z., Provost, C., Villacieros-Robineau, N., Sennechael, N., Garric, G., & Gascard, G.-C. (2017). The Yermak Pass Branch: A major pathway for the Atlantic water north of Svalbard? *Journal of Geophysical Research: Oceans*, *122*, 9332–9349. https://doi.org/10.1002/2017JC013271

Lavergne, T., Eastwood, S., Teffah, Z., Schyberg, H., & Breivik, L. A. (2010). Sea ice motion from low-resolution satellite sensors: An alternative method and its validation in the Arctic. *Journal of Geophysical Research*, *115*, C10032. https://doi.org/10.1029/2009jc005958

Lind, S., Ingvaldsen, R. B., & Furevik, T. (2018). Arctic warming hotspot in the northern Barents Sea linked to declining sea ice import. *Nature Climate Change*, *8*(7), 634–639. https://doi.org/10.1038/s41558-018-0205-y

Maréchal, D. (2004). A soil-based approach to rainfall-runoff modeling in ungauged catchments for England and Wales. PhD Thesis. Cranfield University.

Maslanik, J. A., Fowler, C., Stroeve, J., Drobot, S., Zwally, J., Yi, D., & Emery, W. (2007). A younger, thinner Arctic ice cover: Increased potential for rapid, extensive sea ice loss. *Geophysical Research Letters*, *34*, L24501. https://doi.org/10.1029/2007gl032043

Melsheimer, C., & Spreen, G. (2019). AMSR2 ASI sea ice concentration data, Arctic, version 5.4 (NetCDF) (July 2012 - December 2018), PANGAEA. https://doi.org/10.1594/PANGAEA.89839

Menze, S., Ingvaldsen, R. B., Haugan, P., Fer, I., Sundfjord, A., Beszczynska-Moeller, A., & Falk-Petersen, S. (2019). Atlantic water pathways along the North-Western Svalbard shelf mapped using vessel-mounted current profilers. *Journal of Geophysical Research: Oceans*, *124*, 1699–1716. https://doi.org/10.1029/2018JC014299

Merkouriadi, I., Cheng, B., Graham, R. M., Rosel, A., & Granskog, M. A. (2017). Critical role of snow on sea ice growth in the Atlantic sector of the Arctic Ocean. *Geophysical Research Letters*, *44*, 10,479–10,485. https://doi.org/10.1002/2017GL075494

Merkouriadi, I., Cheng, B., Hudson, S., & Granskog, M. (2020). Effect of frequent winter warming events (storms) and snow on sea-ice growth—A case from the Atlantic sector of the Arctic Ocean during the N-ICE2015 campaign. *Annals of Glaciology*, 1–7. https://doi.org/10.1017/aog.2020.25Meyer

Merkouriadi, I., Gallet, J.-C., Graham, R. M., Liston, G. E., Polashenski, C., Rösel, A., & Gerland, S. (2017). Winter snow conditions on Arctic sea ice north of Svalbard during the Norwegian young sea ICE (N-ICE2015) expedition. *Journal of Geophysical Research: Atmospheres*, *122*, 10,837–10,854. https://doi.org/10.1002/2017JD026753

Merkouriadi, I., Liston, G. E., Graham, R. M., & Granskog, M. A. (2020). Quantifying the potential for snow-ice formation in the Arctic Ocean. *Geophysical Research Letters*, *47*, e2019GL085020. https://doi.org/10.1029/2019GL085020

Meyer, A., Fer, I., Sundfjord, A., & Peterson, A. K. (2017). Mixing rates and vertical heat fluxes north of Svalbard from Arctic winter to spring. *Journal of Geophysical Research: Oceans*, *122*, 4569–4586. https://doi.org/10.1002/2016JC012441

Meyer, A., Fer, I., Sundfjord, A., Peterson, A. K., Smedsrud, L. H., Muilwijk, M., & Kusse-Tiuz, N. (2016). N-ICE2015 ocean microstructure profiles (MSS90L) [Data set]. *Norwegian Polar Institute*. https://doi.org/10.21334/npolar.2016.774bf6ab

Meyer, A., Sundfjord, A., Fer, I., Provost, C., Villacieros Robineau, N., Koenig, Z., et al. (2017). Winter to summer oceanographic observations in the Arctic Ocean north of Svalbard. *Journal of Geophysical Research: Oceans*, *122*, 6218–6237. https://doi.org/10.1002/2016JC012391

Millero, F. J., & Poisson, A. (1981). International one-atmosphere equation of state of seawater. *Deep-Sea Research*, *28A*(6), 625–629.

Muilwijk, M., Smedsrud, L. H., Ilicak, M., & Drange, H. (2018). Atlantic water heat transport variability in the 20th century Arctic Ocean from a global ocean model and observations. *Journal of Geophysical Research: Oceans*, *123*(11), 8159–8179. https://doi.org/10.1029/2018JC014327

Nash, J. E., & Sutcliffe, J. F. (1970). River flow forecasting through conceptual models. Part I—A discussion of principles. *Journal of Hydrology*, *10*, 282–290.

Notz, D. (2005). Thermodynamic and Fluid-Dynamical Processes in Sea Ice. PhD thesis, University of Cambridge, UK.

Onarheim, I. H., Smedsrud, L. H., Ingvaldsen, R. B., & Nilsen, F. (2014). Loss of sea ice during winter north of Svalbard. *Tellus Series a-Dynamic Meteorology and Oceanography*, *66*, 23933. https://doi.org/10.3402/Tellusa.V66.23933

OSPAR Commission (1998). Report of the Modeling Workshop on eutrophication issues. 5–8 November 1996. Den Haag, The Netherlands. OSPAR Report, 86 pp.

Padman, L., Plueddemann, A. J., Muench, R. D., & Pinkel, R. (1992). Diurnal tides near the Yermak Plateau. *Journal of Geophysical Research*, *97*(C8), 12,639–12,652. https://doi.org/10.1029/92jc01098

Peterson, A. K., Fer, I., McPhee, M. G., & Randelhoff, A. (2017). Turbulent heat and momentum fluxes in the upper ocean under Arctic sea ice. *Journal of Geophysical Research: Oceans*, *122*, 1439–1456. https://doi.org/10.1002/2016JC012283

Peterson, A. K., Fer, I., Randelhoff, A., Meyer, A., Håvik, L., Smedsrud, L. H., McPhee, M.G. (2016). N-ICE2015 ocean turbulent fluxes from under-ICE turbulence cluster (TIC) (data set), Norwegian Polar Institute. https://doi.org/10.21334/npolar.2016.ab29f1e2

Polyakov, I. V., Pnyushkov, A. V., Alkire, M. B., Ashik, I. M., Baumann, T. M., Carmack, E. C., et al. (2017). Greater role for Atlantic inflows on sea ice loss in the Eurasian Basin of the Arctic Ocean. *Science*, *356*(6335), 285–291. https://doi.org/10.1126/science.aai8204

Polyakov, I. V., Pnyushkov, A. V., Rember, R., Padman, L., Carmack, E. C., & Jackson, J. M. (2013). Winter convection transports Atlantic water heat to the surface layer in the eastern Arctic Ocean. *Journal of Physical Oceanography*, *43*(10), 2142–2155. https://doi.org/10.1175/Jpo-D-12-0169.1

Provost, C., Sennéchael, N., Miguet, J., Itkin, P., Rösel, A., Koenig, Z., & Granskog, M. A. (2017). Observations of flooding and snow-ice formation in a thinner Arctic sea ice regime during the N-ICE2015 campaign: Influence of basal ice melt and storms. *Journal of Geophysical Research: Oceans*, *122*, 7115–7134. https://doi.org/10.1002/2016JC012011

Radach, G., & Moll, A. (2006). Review of three-dimensional ecological modeling related to the North Sea shelf system. Part II: Model validation and data needs. *Oceanography and Marine Biology: An Annual Review*, *44*, 1–60. https://doi.org/10.1201/9781420006391

Renner, A. H. H., Sundfjord, A., Janout, M. A., Ingvaldsen, R. B., Beszczynska-Mõller, A., Pickart, R. S., & Perez-Hernandez, M. D. (2018). Variability and redistribution of heat in the Atlantic water boundary current north of Svalbard. *Journal of Geophysical Research: Oceans*, *123*, 6373–6391. https://doi.org/10.1029/2018JC013814

Ricker, R., Hendricks, S., Kaleschke, L., Tian-Kunze, X., King, J., & Haas, C. (2017). A weekly Arctic sea ice thickness data record from merged CryoSat-2 and SMOS satellite data. *The Cryosphere*, *11*(4), 1607–1623. https://doi.org/10.5194/tc-11-1607-2017

Rinke, A., Maturilli, M., Graham, R. M., Matthes, H., Handorf, D., Cohen, L., et al. (2017). Extreme cyclone events in the Arctic: Wintertime variability and trends. *Environmental Research Letters*, *12*(9), 094006. https://doi.org/10.1088/1748-9326/Aa7def

Rösel, A., Divine, D., King, J. A., Nicolaus, M., Spreen, G., Itkin, P., Granskog, M.A. (2016). N-ICE2015 total (snow and ice) thickness data from EM31 (v1.0) (data set). Norwegian Polar Institute. https://doi.org/10.21334/npolar.2016.70352512

Rösel, A., Itkin, P., King, J., Divine, D., Wang, C., Granskog, M. A., et al. (2017). This sea ice, thick snow and widespread negative freeboard observed during N-ICE2015 north of Svalbard. *Journal of Geophysical Research: Oceans*, *123*, 1156–1176. https://doi.org/10.1002/2017JC012865

Rösel, A., & King, J. (2017). N-ICE2015 ice thickness, snow thickness, and freeboard from thickness drillings (data set). Norwegian Polar Institute. https://doi.org/10.21334/npolar.2017.25f70db1

Rudels, B., Meyer, R., Fahrbach, E., Ivanov, V. V., Østerhus, S., Quadfasel, D., et al. (2000). Water mass distribution in Fram Strait and over the Yermak Plateau in summer 1997. *Annales Geophysicae*, *18*(6), 687–705. https://doi.org/10.1007/s005850000216

Schauer, U., Fahrbach, E., Osterhus, S., & Rohardt, G. (2004). Arctic warming through the Fram Strait: Oceanic heat transport from 3 years of measurements. *Journal of Geophysical Research*, *109*, C06026. https://doi.org/10.1029/2003jc001823

Spielhagen, R. F., Werner, K., Sorensen, S. A., Zamelczyk, K., Kandiano, E., Budeus, G., et al. (2011). Enhanced modern heat transfer to the Arctic by warm Atlantic water. *Science*, *331*(6016), 450–453. https://doi.org/10.1126/science.1197397

Spreen, G., Kaleschke, L., & Heygster, G. (2008). Sea ice remote sensing using AMSR-E 89-GHz channels. *Journal of Geophysical Research*, *113*, C02S03. https://doi.org/10.1029/2005jc003384

Spreen, G., Kwok, R., & Menemenlis, D. (2011). Trends in Arctic sea ice drift and role of wind forcing: 1992–2009. *Geophysical Research Letters*, *38*, L19501. https://doi.org/10.1029/2011gl048970

Stroeve, J. C., Kattsov, V., Barrett, A., Serreze, M., Pavlova, T., Holland, M., & Meier, W. N. (2012). Trends in Arctic sea ice extent from CMIP5, CMIP3 and observations. *Geophysical Research Letters*, *39*, L16502. https://doi.org/10.1029/2012gl052676

Taskjelle, T., Hudson, S. R., Pavlov, A., & Granskog, M. A. (2016). N-ICE2015 surface and under-ice spectral shortwave radiation data (data set), Norwegian Polar Institute. https://doi.org/10.21334/npolar.2016.9089792e

Tetzlaff, A., Lupkes, C., Birnbaum, G., Hartmann, J., Nygard, T., & Vihma, T. (2014). Brief communication: Trends in sea ice extent north of Svalbard and its impact on cold air outbreaks as observed in spring 2013. *The Cryosphere*, *8*(5), 1757–1762. https://doi.org/10.5194/tc-8-1757-2014

Tschudi, M., Meier, W. N., Stewart, J. S., Fowler, C., & Maslanik, J. (2019). Polar pathfinder daily 25 km EASE-Grid sea ice motion vectors, version 4. Boulder, Colorado USA. NASA National Snow and Ice Data Center Distributed Active Archive Center. https://doi.org/10.5067/INAWUWO7QH7B. [date accessed].

Turner, A. K., Hunke, E. C., & Bitz, C. M. (2013). Two modes of sea ice gravity drainage: A parameterization for large-scale modeling. *Journal of Geophysical Research: Oceans*, *118*, 2279–2294. https://doi.org/10.1002/jgrc.20171

Unesco (1983). Algorithms for computation of fundamental properties of seawater. *Unesco Tech. Pap. in Mar. Sci._, No. 44*, 53 pp.

Urrego-Blanco, J. R., Urban, N. M., Hunke, E. C., Turner, A. K., & Jeffery, N. (2016). Uncertainty quantification and global sensitivity analysis of the Los Alamos sea ice model. *Journal of Geophysical Research: Oceans*, *121*, 2709–2732. https://doi.org/10.1002/2015JC011558

Walczowski, W., & Piechura, J. (2011). Influence of the West Spitsbergen Current on the local climate. *International Journal of Climatology*, *31*(7), 1088–1093. https://doi.org/10.1002/joc.2338

Walden, V. P., Hudson, S. R., Cohen, L., Murphy, S. Y., & Granskog, M. A. (2017). Atmospheric components of the surface energy budget over young sea ice: Results from the N-ICE2015 campaign. *Journal of Geophysical Research: Atmospheres*, *122*, 8427–8446. https://doi.org/10.1002/2016JD026091

Walden, V. P., Murphy, S., Hudson, S. R., & Cohen, L. (2017). N-ICE2015 atmospheric turbulent fluxes (data set). Norwegian Polar Institute. https://doi.org/10.21334/npolar.2017.298013b7

Warren, S. G., Rigor, I. G., Untersteiner, N., Radionov, V. F., Bryazgin, N. N., Aleksandrov, Y. I., & Colony, R. (1999). Snow depth on Arctic sea ice. *Journal of Climate*, *12*(6), 1814–1829. https://doi.org/10.1175/1520-0442(1999)012<1814:Sdoasi>2.0.Co;2